Scenario-based assessment of buildings damage and population exposure due to earthquake-induced tsunamis for the town of Alexandria, Egypt

Pagnoni G., Armigliato A. and Tinti S.

Sector of Geophysics, Department of Physics and Astronomy (DIFA), University of Bologna, Italy (gianluca.pagnoni3@unibo.it, tel. +39 051 2095165, fax +39 051 2095058)

Abstract

Alexandria is the second biggest city in Egypt as regards population, is a key economic area in northern Africa and has a very important tourist activity. Historical catalogues indicate that it was severely affected by a number of tsunami events. In this work we assess the tsunami hazard by running numerical simulations of tsunami impact in Alexandria through the Worst-case Credible Tsunami Scenario Analysis (WCTSA). We identify three main seismic sources: the Western Hellenic Arc (WHA - reference event 365 AD, Mw=8.5), the Eastern Hellenic Arc (EHA - reference event 1303, Mw=8.0) and the Cyprus Arc (CA - hypothetical scenario earthquake with Mw=8.0), inferred from the tectonic setting and from historical tsunami catalogues. All numerical simulations are carried out in two sea level conditions (mean sea level and maximum high-tide sea level) by means of the code UBO-TSUFD, developed and maintained by the Tsunami Research Team of the University of Bologna. Relevant tsunami metrics are computed for each scenario and then used to build aggregated fields such as the maximum flood depth and the maximum inundation area. We find that the case that produces the most relevant flooding in Alexandria is the EHA scenario, with wave heights up to 4 m. The aggregate fields are used for a building vulnerability assessment according to a methodology developed in the frame of the EU-FP6 project SCHEMA and further refined in this study, based on the adoption of a suitable building damage matrix and on water inundation depth. It is found that in the districts of El Dekhila and Al Amriyah, to the south-west of the port of Dekhila over 12,000 (13,400 in case of the maximum high-tide) buildings could be affected and hundreds of them could incur in consequences ranging from important damage to total collapse. It is also found that in the same districts tsunami inundation covers an area of about 15 km^2 resulting in more than 150,000 (165,000 in case of the maximum high tide) residents being exposed.

1   **Introduction**

2   The main objective of this study is to assess the damage to buildings in Alexandria,

3   Egypt, due to tsunami inundation, as well as the amount of affected population. In the paper we

4   restrict our attention to tsunamis induced by earthquakes, that constitute the major threat for the

5   town and adopt the approach based on tsunami scenarios. Alexandria is one of the oldest cities

6   in the world, founded in 331 B.C. by Alexander the Great close to the Egyptian port of Rakotis

7   that was already known in Homeric times, and remained the capital of Egypt for over 1000

8   years. Administratively, Alexandria governorate consists of one big town, i.e. Alexandria with

9   about 4.1 million people, and two small cities, namely Borg El Arab City and New Borg El

10 Arab, all together forming the Metropolitan Alexandria. The governorate of Alexandria counts

11 a population of about 4.8 million. Today, Alexandria is one of the major cities in the

12 Mediterranean sea, developing along a narrow strip of coast about 70 km long, separating the

13 Mediterranean sea from the inner 75 km^2 Lake Maryut (with ancient name Mareotis). The city

14 of Alexandria is considered the Egypt's second capital by virtue of its location and population

15 size. During summer months, the city receives some 3 million visitors (it was a mere 309,000

16 in 2002), making it the most popular summer resort for Egyptians. The total area of Alexandria

17 is 2680 km^2, divided into six districts that from NE to SW are (see Fig. 1): Al-Montazah, Sharq

18 (Eastern Alexandria), Al-Gomrok, which is the historic old town, Wassat (Central Alexandria),

19 El-Dekhila-Agami (Western Alexandria) and Al-Amriyah, the first 5 sitting on the coast, and

20 the last one being more in the interior.

21 Alexandria plays a key role in the national economy: the port of Alexandria is the

22 Egypt's largest, with 57% of the total port capacity in the country, and one of the major ports

23 in the Mediterranean basin. In the paper (Fig. 1) we will denote the Ras El Tin harbour, that is

24 mainly for yachting and fishing boats and is not navigable by large vessels, as the Eastern Port

25 of Alexandria. This is the place where the ancient Great Harbour of Alexandria was located, as

26 testified by submerged port structure remains identified by archeologists. The harbour is

27 protected by a breakwater system with an average height of 3 m asl leaving two entrances of ~

28 240 m (west) and ~ 140 m (east) width. Further, the harbour basin between Ras El Tin and

29 Wassat will be considered as formed by two ports denoted as the port of Dekhila to the west

30 and the Western Port of Alexandria to the east, which is the most important port facility of the

31 region. The port of Dekhila defense system is formed by two joint breakwaters: one parallel to

32 the coast about 2250 m long and the other, more recent, ~ 600 m long, having an average height

33 of 4 m asl and of 1.5 m asl at the head zone. Notice that the Eastern and Western Ports of

34 Alexandria are separated by a "tombolo", i.e. by a narrow strip of land or isthmus connecting

35 the mainland with the former island of Pharos, that today forms a T-shaped peninsula. From its

36 western end, a 2400 m long and shallow (~ 2 m asl) breakwater, striking mostly N-S, leaves an

37 about 400 m entrance to ship traffic. Close to the harbour area one can find also one of the most

38 important industrial districts in Egypt, with several large, well-equipped industrial plants (e.g.

39 Borg El Arab, Merghem, Om Zegheow and El Gharbaneyyat) that give it a dominant position

40 in the manufacturing sector. Other industrial sectors are very important: chemical and

41 petrochemical, steel, iron and engineering industries, construction materials, wood products,

42 food industries, etc.

43   From a physiographic point of view, the city of Alexandria lies on a series of narrow

44 Late Pleistocene ridges running parallel to the coast separating the sea from the very shallow

45 Lake Maryut, that is one of the many lagoons and marshes characterizing the vast area of the

46 Nile delta. These brackish lakes are connected to the sea by a complex system of artificial

47 waterways, two of which, the Alexandria and the Al-Max channels, drain the waters of the Lake

48 Maryut into the Alexandria harbour basin also by means of pumping stations, between the port

49 of Dekhila and the Western Port of Alexandria in the district of Wassat.

50   Alexandria was hit by a number of tsunamis in the course of the history (see

51 Papadopoulos et al. 2007; Salamon et al. 2007), two of which have flooded the city with

52 destructive effects, namely the 21 July 365 AD and the 8 August 1303 Crete tsunami events.

53 The detailed reconstruction of these tsunamis is out of the scope of this paper. We will only

54 recall their most relevant features in the following.

55

56 The 365 AD Tsunami

57   The 365 AD earthquake and tsunami were first described by coeval sources. Ammianus

58 Marcellinus (see Guidoboni et al. 1994; Stiros 2001), a Roman historian who lived in the fourth

59 century (325-391 AD), writes in 378, that is 13 years after the event occurrence, that the earth

60 was shaken by an earthquake and then a tsunami brought destruction to ships in the sea and to

61 people on land. He speaks of a strong sea withdrawal and return, of several thousands of people

3

62   drawn mainly because they were surprised unexpectedly by the returning water, of vessels

63   landed on roofs, and of some other vessels carried on land more than two miles from the

64   coastline. Indeed, Ammianus Marcellinus does not refer all the above occurrences to any

65   specific geographical locations, apart from two exceptions: 1) he mentions Alexandria on

66   speaking of ships that were left on house roofs ("… *Ingentes aliae naves, extrusae rabidis*

67   *flatibus culminibus insedere tectorum, ut Alexandriæ contigit, …" Other big vessels pushed out*

68   *of the sea by the fury of winds ended onto the top of roofs, which occurred in Alexandria…*)

69   and 2) he mentions Methoni, a town in Messenia, southern Peloponnese, Greece, on reporting

70   of ships transported about two miles onshore ("… *ad secundum lapidem fere procul a litore*

71   *contortæ sunt aliquæ, ut Laconicam prope Mothonem oppidum nos transeundo conspeximus,*

72   *diuturna carie fatiscentem …" Some vessels were carried up to two miles away from the coast,*

73   *as I saw one from Sparta dilapidated for a long decay while I was travelling near the town of*

74   *Methoni*). Therefore, his description, although quite realistic, cannot be used for a modern

75   reconstruction. From later sources it seems that most of Alexandria escaped destruction and

76   that damage was confined to the narrow causeway connecting the town to the island of Pharos,

77   where the famous lighthouse, one of the seven wonders of the world, was built (Shaw 2008;

78   Stiros 2010). It was called Eptastadion (Pararas-Carayannis 2011) since its length was about 7

79   stadia (a stadium is an ancient Greek distance unit equal to 184.45 m) and the tombolo that

80   formed on it divides today the East from the West Port of Alexandria in the district of Al-

81   Gomrok (see the locality Ras el Tin in Fig. 1). Recent studies agree that the 365 AD shock was

82   a large magnitude (Mw 8.3-8.5) earthquake that occurred in the Hellenic subduction zone

83   between southwestern Crete and the Peloponnese (e.g. Stiros 2010). Uplifts up to 10 m of the

84   coast in western Crete were recognised, identified and dated (Pirazzoli et al. 1992, 1996; Shaw

85   et al. 2008) and, as for today, are the main clue to placing the source of this tsunami in the

86   WHA. In this study an AD 365-like tsunami is one of the Worst-case Credible Scenarios we

87   use to evaluate the tsunami vulnerability of Alexandria.

88

89   The 1303 Tsunami

90   The 8 August 1303 earthquake was destructive over a vast area of the eastern

91   Mediterranean and also the ensuing tsunami caused a widespread damage in many countries

92   including Egypt. According to several studies, that also consider Arab documentary sources

93   (e.g. Ambraseys et al. 1994; Guidoboni and Comastri 1997, 2005; El Sayed et al. 2000) the

94   most severe earthquake destruction was suffered by Candia (Heraklion today), Crete, but also

95   Peloponnese towns were affected. Intense damage was reported in Cyprus, Palestine (city of

96   Safad), and also in Egypt where Cairo and Alexandria resulted to be severely hit: in Alexandria

97   the city walls and the lighthouse partially collapsed and many houses were ruined. The area of

98   the reported damage was so large that some were induced to doubt that it was a unique event

99   and to hypothesize that historical accounts put together effects of a series of earthquakes

100   occurred in different seismic zones. There is a general consensus that the earthquake (or the

101   bigger earthquake in case of a multiple source scenario) occurred in the EHA with Mw around

102   8.0 (Papadopoulos et al. 2014).

103   Effects of the tsunami are reported in several coeval sources with explicit reference to

104   the towns of Candia (Heraklion), Crete, for Italian sources, and of Acre (Israel), Alexandria and

105   Nile for Arab sources. In Alexandria, vessels broke moorings in the harbour and crashed against

106   rocks, the tsunami reached the town walls and many shops and warehouses were flooded and

107   destroyed (Ambraseys 1962; Antonopoulos 1980; Guidoboni and Comastri 1997; El Sayed et

108   al. 2000; Papadopoulos et al. 2007; Papadopoulos 2011).

109   In this study, a 1303-like tsunami with source in the EHA is considered as one of the

110   Worst-case Credible Tsunami Scenarios.

111

The Worst-case Credible Tsunami Scenario Analysis (WCTSA)

113   Tsunami scenarios are used as a tool to plan the immediate response of coastal

114   communities to a tsunami attack by emergency managers in the context of tsunami early

115   warning systems, as well as to carry out hazard, vulnerability and risk analyses in the frame of

116   long-term mitigation policy planning. In this latter case, scenario-based techniques are often

117   seen as a means that is alternative or complementary to probabilistic approaches. A typical

118   product of a probabilistic tsunami hazard analysis (PTHA) is the inundation area or the

119   maximum sea surface elevation that are expected in a given place (stretch of coastline, port,

120   beach, etc.) in a given return period, say 100 or 500 yrs. The method is essentially mimicked

121   from the probabilistic analysis applied to earthquakes and was first suggested in early '80s by

122   Lin and Tung (1982). The concept was independently developed and applied to evaluate the

123   maximum expected wave at the coast in the Italian seas by Tinti (1991a, 1991b) and in Morocco

124   by El Alami and Tinti (1991), but it is only in more recent times that it was fully developed,

125   discussed and extensively applied (see e.g. Geist and Parson 2006; Burbidge et al. 2008; Lorito

126 et al. 2008; Gonzalez at al. 2009; Sørensen et al. 2012; Leonard et al. 2014; Brizuela et al. 2014,

127 Lorito et al. 2015). The main drawback of this method is that it relies upon the occurrence

128 probability distribution function of the tsunamigenic sources, that cannot always be estimated

129 reliably, especially if submarine mass failures are involved. Therefore, it is often restricted to

130 application where only tsunami of seismic origin are taken into account, with only rare

131 exceptions (see Grilli et al. 2009).

132   The scenario-based approach stands on the idea that in many applications concerning

133 tsunami mitigation what matters most is not the knowledge of the effects of a full spectrum of

134 tsunami events with associated probability of occurrence, but only the knowledge of the features

135 of the extreme events. Typically in a given coastal place one wants to assess the most extended

136 inundation area due to tsunamis, the maximum tsunami height, etc. In principle, one could

137 derive this information from a PTHA by considering longer and longer return times, but it is

138 more practical to avoid all the probability assessment complications and consider only the

139 largest sources and therefore the largest produced tsunamis. The main steps of the scenario-

140 based hazard analysis can be summarized as follows: 1) identification and characterization of

141 the sources (earthquakes, volcanos, landslides) capable of producing the largest tsunamis for a

142 given target location, 2) simulation of the tsunamis and computation of the desired metrics in

143 the target place, 3) computation of the local aggregate (envelope) scenario by combining all the

144 individual scenarios. This method can be called the method of the Probable Maximum Tsunami

145 (PMT) (see Grilli et al. 2011) or equivalently the method of the Worst-case Credible Tsunami

146 (WCT) (see Tonini et al. 2011). It is noted that the specifications "probable" and "credible" in

147 these locutions means i) that the scenarios considered are reasonably grounded on scientific

148 acceptable assumptions (e.g. the maximum possible earthquake size of a given seismic zone)

149 and ii) that very improbable scenarios are ruled out (e.g. the impact of a meteorite or asteroid

150 in the sea just off the target place), which is a possible catastrophic case, but with an extremely

151 low probability of occurrence.

152   The above steps lead to the computation of an envelope or aggregate scenario in a given

153 place that forms the basis for the subsequent studies. In particular, in this paper we estimate the

154 maximum area of inundation for the governorate of Alexandria and then we evaluate the

155 exposure, vulnerability and damage of the buildings in the residential area and the number of

156 affected people.

157

The Selected Tsunamigenic Sources

Seismotectonics focused on tsunami activity and potential in the eastern Mediterranean has been the subject of several recent works with regional and also local character (see Soloviev et al. 2000; Tinti et al. 2005; Fokaefs and Papadopoulos 2007; Papadopoulos et al. 2007; Salamon et al. 2007; Lorito et al. 2008; Ebeling et al. 2012; Sørensen et al. 2012; Yolsal-Çevikbilen and Taymaz 2012). Most of these works were mainly concentrated on tsunamis generated by earthquakes, but also tsunamis due to landslides are of some relevance in the region. Indeed, it is known (Fokaefs and Papadopoulos 2007; Salamon et al. 2007; Papadopoulos et al. 2014) that tsunamis that occurred off Syria, Lebanon, Israel and Palestine, and that are associated with earthquakes in the Dead Sea Transform fault, have been attributed to submarine sediment failures triggered by seismic load rather than to the sea floor deformation caused by earthquakes (since faults are too far from the sea and with mechanism unfavorable to tsunamigenesis). Numerical simulations of tsunamis induced by these submarine mass failures (see the tsunami following a 1.25 km^3 volume collapse in the Akhziv submarine canyon, 30 km north of Haifa in Salamon et al. 2007) show that their effects may be disastrous near the source, but are minor in the far field. For this main reason, we restrict our attention only to scenarios of tsunamis caused by earthquakes in the present study. It is worth mentioning here also the work by Garziglia et al. (2007) who studied a huge, about 14 km^3, mass-transport deposit, called S16, that was triggered during the Holocene sea-level rise circa 10 kyr BP in the western Nile margin in correspondence with exceptional river sediment supplies. Consequently, they simulated a tsunami with a source only some 50 kilometers north of Alexandria. The numerical simulations show that waves with height of 4 meters can attack the coast (Garziglia et al. 2007). However, our evaluation is that probably the mass transport was too slow to generate a tsunami and that, even accepting that it was tsunamigenic, it is a scenario by far less probable to occur today than scenarios of tsunamis of seismic origin. Therefore, in the following we do not take it into account.

Considering all the main tsunamigenic seismic zones of the Mediterranean, Sørensen et al. (2012) were able to show that the sources that are most influential for the area of Alexandria are essentially the EHA and the WHA. Following their suggestion, and on the basis of the tsunami history showing that the largest tsunamis known to have hit the town were due to the 365 AD earthquake in the WHA and to the 1303 earthquake in the EHA, we selected two scenarios with faults represented in Fig. 2 and with geometry and focal mechanism given in Table 1. The magnitudes of the scenario earthquakes are compatible with the ones taken by

7

190   Sørensen et al. (2012). More in detail, the selected WHA source coincides with the fault

191   introduced by Lorito et al. (2008), characterized by an Mw=8.5. Instead, the geometry of the

192   EHA source is borrowed from the paper by Yolsal-Çevikbilen and Taymaz (2012), but the

193   position of the fault is chosen in order to maximize the tsunami propagation effect towards

194   Alexandria.

195   In addition to the above cases, we explore also a third scenario, that is a tsunami of

196   seismic origin from a fault in the Cyprus Arc (CA). The reason is that this zone is known to be

197   tsunamigenic (Fokaefs and Papadopoulos 2007) and to be susceptible to large magnitude

198   earthquakes. We assume a Mw=8.0 earthquake, not far from the assumption made by Salamon

199   et al. (2007) who take Mw=7.8, while Sørensen et al. (2012) and Papadopoulos et al. (2014)

200   estimate a maximum magnitude for this area of Mw=7.5. Further, the position and strike of the

201   fault in the present study (see Fig. 2 and Table 1) is selected in such a way to maximize tsunami

202   effects on the Egypt coasts, while a similar case treated by Salamon et al. (2007) was assumed

203   in a different location along the arc, with a strike more suitable to direct most of the tsunami

204   energy against Israel.

205

206   **Tsunami Simulations**

207   Tsunami simulations have been conducted by using the code UBO-TSUFD that solves

208   shallow-water non-linear equations with dynamic boundary conditions and a finite difference

209   technique, where the unknowns are the sea surface elevation with respect to the still sea level

210   and the two horizontal fluxes or discharges, i.e. the product of the sea surface elevation by the

211   particle horizontal velocity components (Tinti and Tonini 2013). The initial conditions for the

212   tsunami scenarios are computed by means of the analytical Okada's formulas for the static

213   deformation of an elastic half-space induced by a uniform co-seismic slip on a rectangular fault

214   (Okada 1992). The hypothesis is that the sea floor vertical displacement is transferred

215   instantaneously and unchanged to the sea surface, which can be considered a quite acceptable

216   assumption. The complementary hypothesis is that the initial horizontal velocity is identically

217   zero. Both such conditions are usual for tsunami simulations, unless more precise knowledge

218   of the rupture process (e.g. dynamic rupture pattern, heterogeneous slip distribution, etc.) is

219   obtained from additional data. Pure transparency is imposed on the open boundaries allowing

220   the tsunami waves to go across the grid limits with no spurious back-reflection, while on the

221 coast an algorithm based on extrapolating the seaside wave profile landward determines if a

222 cell is wet or dry and the shoreline position is computed dynamically (Tinti and Tonini 2013).

223   To ensure that the model computes adequately the tsunami interaction with the irregular

224 coast in the target place (i.e. Alexandria) and at the same time to optimize computer resources,

225 the strategy of nested grids is adopted by the code UBO-TSUFD with a full-coupling between

226 the outer (coarser) and the inner (finer) grid. Usually, the finer grid is totally contained within

227 the outer grid, and this is the case for the scenarios treated in this paper, but this is not a

228 requirement of the code. Notice that in the area of overlapping, that is common to both grids,

229 computations are carried out only in the finer grid. Technically, if we consider a multilevel

230 nesting with level N+1 grids nested in the grid of level N, the computation domain of the level

231 N grid is the one obtained as the difference between the area covered by the grid and the area

232 that is the union of all grids at level N+1. In total, the grid system in this work is formed by four

233 grids, from level 1 to level 4, that are shown in Fig. 2. The external grid, at level 1, covers all

234 the eastern Mediterranean sea with a 3 km resolution and is large enough to contain the faults

235 of all tsunami scenarios as well as the respective tsunami initial conditions. Since the

236 deformation produced by Okada's equations decays quite slowly with the distance from the

237 fault (which results in an initial tsunami source virtually extending up to infinity), sea elevations

238 in magnitude less than 5 cm have been put equal to zero, and a proper tapering window has

239 been used to avoid discontinuities. The modified initial fields are given in Fig. 2. The second

240 grid, grid 2, covers the south-eastern part of the Levantine sea with a 1 km resolution. Grid 3

241 (200 m resolution) and grid 4 (40 m resolution) cover a much smaller area and are centered

242 respectively on the governorate of Alexandria and on Alexandria city, that is the study area in

243 this paper.

244   The topo-bathymetric data sets used to build the grids are listed in Table 2. Grids 1 and

245 2 have been built by using basically GEBCO (30 arcsec) and SRTM (~90 m) databases. The

246 local grids 3 and 4 have been integrated with bathymetry data in UTM coordinates from nautical

247 charts (1:5000 and 1:10000), and also from the work by El-Geziry et al. (2007) for the Western

248 Port of Alexandria, while SRTM topography has been cross-checked with Google Earth data in

249 selected control points. Specific attention has been posed to reconstructing the shoreline

250 position and the shape of breakwaters and jetties in the ports of Alexandria and Dekhila by

251 making use of Google Earth images. It is worth mentioning that bathymetry of the different

252 grids have to be harmonized along and in the neighborhood of the common boundaries,

253 especially in near-shore regions to avoid artificial depth discontinuities that might give rise to

254 irregular wave behavior even resulting in numerical instabilities.

255 All simulations have been carried out for two different sea-level conditions: mean sea

256 level and the maximum high-tide level. The tidal range in the Alexandria is about 60 cm (see

257 the analysis by El-Geziry and Radwan, 2012, who examined the 1996-2005 decade records of

258 the Western Port tide-gage). Accordingly, we assume in the paper that the highest high-tide sea

259 level exceeds the mean sea level by 30 cm. The maximum high-tide bathymetry and topography

260 have been obtained by lowering by 30 cm the depth of the sea floor and the altitude of the dry

261 land in the local grid 4 centered on the Alessandria coast and ports. The assumption is that tides

262 are not relevant for tsunami propagation offshore, but only in the nearshore region. All the

263 results shown in detail in the following sections refer to the mean-sea-level condition, while

264 results for the maximum high-tide level are summarized in the Appendix A2.

265

266 The WHA Tsunami

267 The WHA earthquake produces a tsunami that focuses most of its energy towards the

268 Libyan coasts and SW-ward (see Fig. 3), whereas only a marginal part of the waves travel

269 towards the eastern Mediterranean. Sea level maxima in the local grid 3 shown in Fig. 4 are

270 above 2.5 m along almost the entire Alexandria governorate coastline, with peaks above 4 m in

271 correspondence with the Borg El Arab area, possibly related to local bathymetric features. We

272 observe that we made reference to the grid number only for the sake of simplicity. To be more

273 precise, when we show the fields in the region of computation covered by the grid of level N,

274 we show at the same time also the fields calculated in all the nested grids at level larger than N.

275 The fact that there is perfect continuity between fields across the grid boundaries as it appears

276 from Figs. 3 and 4 is a demonstration of the good performance of the code UBO-TSUFD. The

277 same comment applies to all other figures of the paper where tsunami fields are represented.

278 Propagation fields depicted in Fig. 5 at intervals of 20 min for the first 140 minutes show the

279 main front travelling quickly towards the south of the central Mediterranean basin. The last four

280 panels of Fig. 5 show the propagation in the Levantine sea over grid 2. The tsunami advances

281 with a leading negative wave attacking Cyprus in the north and Alexandria in the south about

282 80 minutes after the earthquake. Notice the strong bending of the southern part of the front to

283 the east of Alexandria due to refraction, with the result that the tsunami front tends to align with

284 the depth isolines and attacks the coast at a normal angle (see the bottom panels of Fig. 5). The

10

285   tsunami produces a relevant flooding of the beaches to the west of Alexandria, of the port of
286   Dekhila, of the Wassat area and of the harbour facilities of the Western Port of Alexandria (Fig.
287   6). The flooding is less evident for the eastern port. In the areas where the inundation distance
288   is larger, flow depth can exceed 2.0-2.5 m. Notice that the WHA scenario tsunami does not
289   flood the tombolo between the Eastern and Western Ports of Alexandria, which was probably
290   inundated by the 365 AD event. This is not, however, a serious drawback of the scenario, since
291   probably the topography today is not the same as at the time of the historical tsunami. What is
292   confirmed is that the tsunami is damaging, although not disastrous for Alexandria.

293

294   The EHA Tsunami

295   The EHA tsunami directs the bulk of its energy towards Alexandria (see Fig. 7). This is
296   mainly due to the assumed strike of the fault, and is a well-known feature of essentially 2D
297   wave processes originating from long linear sources. The beam of sea level maxima is
298   orthogonal to the fault and is strong along the entire path from the source to the Alexandria
299   coasts where they amplify. The zoom on the area of Alexandria (see grid 3 represented in Fig.
300   8) shows that maxima may exceed 2 m offshore and that tsunami causes extended inundation
301   all along the town coast from SW to NE. The propagating front is shown in the snapshots of
302   Fig. 9. From panels at 20 and 40 min it is clear that the tsunami travels with a leading positive
303   wave towards Alexandria. The panel at 1h shows the strong interaction of the tsunami with the
304   continental margin, causing the strong bending of the front and the remarkable shortening of
305   the wavelength (with crests and troughs coming closer to each other). The snapshot at 1h 20
306   min shows that the front is very strong not only in Alexandria, but even in the whole region to
307   the east of the town, that indeed is covered only by the 1 km resolution grid 2. The inundation
308   in the town of Alexandria is depicted in Fig. 10 (grid 4). It is seen that most of the coast is
309   flooded and in some zones the tsunami penetrates a few kilometers deep in the interior beyond
310   the coastal ridge. Flooding in the area of the old port of Alexandria (Ras El Tin) is noticeable,
311   but not dramatic: the outer breakwaters of both Eastern and Western Ports of Alexandria are
312   overtopped and the harbour facilities together with the waterfront buildings are inundated. This
313   is compatible with the effects reported for the 1303 tsunami mentioned in one of the previous
314   sections.

315

316   The CA Tsunami

317   The source located in the CA is by purpose taken in a position of the arc with strike
318   launching most of the tsunami energy towards the Egyptian coast. The pattern of the sea surface
319   elevation maxima (Fig. 11) displays the effect of the Eratosthenes seamount, a ~2000 m high
320   massif south of the fault, that amplifies the tsunami and concentrates it against the eastern part
321   of the Nile delta where extensive flooding is computed in the area of Damietta and Port Said
322   (grid 2), quite far from Alexandria. In the shelf off Egypt the structure of the maxima is complex
323   and one can observe amplified branches even on the western part of the Nile delta just to the
324   east of Alexandria. In the large Alexandria region, however, the tsunami extreme elevations are
325   only in the range of 1.0-1.5 m near the coast (Fig. 12). The tsunami propagation frames shown
326   in Fig. 13 display a concentration and splitting of the tsunami front (a positive leading wave)
327   induced by the Eratosthenes massif that attacks the Egypt coast with a long double crest system
328   (see tsunami elevation fields taken at 1h and following times). Fig. 14 shows that flooding in
329   Alexandria is somewhat less pronounced than for the WHA and the EHA scenarios: the largest
330   effects are observed in the Dekhila port area.

331   The simulation shows that CA tsunami scenario foresees moderate flooding in
332   Alexandria and severe flooding in the eastern part of the Nile delta. Going through tsunami
333   catalogues and specialized literature one can find mention of a few tsunamis flooding this area.
334   The most interesting for our study is the tsunami associated to an earthquake that occurred
335   between 26 and 17 BC and caused severe damage in Paphos, Cyprus (Guidoboni et al. 1994).
336   The earthquake generated a tsunami that hit Cyprus, but also the town of Pelusium on the
337   eastern side of the Nile delta according to some studies (Altinok and Ersoy 2000; Fokaefs and
338   Papadopoulos 2007; Altinok et al. 2011), or the entire coast from Alexandria to Pelusium
339   according to others (Ambraseys 1962). Considering that Pelusium was one of the most
340   important towns of the Lower Egypt that was located to the east of the today Port Said, one can
341   see that the inundation associated with the CA tsunami scenario seems reasonably consistent
342   with the historical data.

343

344   Virtual Tide Gauges

345   Time histories of the sea surface elevations calculated for some virtual tide gauges, i.e.
346   computed in some nodes of the simulation grids, may help to understand better the tsunami
347   dynamics. To this purpose we have selected four nodes in grid 4 (that has the highest
348   resolution). Tide gauge 1 is placed some 15 km offshore and the others are placed very close to

349   the coast in less than 10 m sea depth. Tide gauges 2 and 4 are in the open sea, to the east and

350   west of Alexandria respectively, while tide gauge 3 is within the port of Dekhila. Their positions

351   can be seen in Fig. 6 and are also reported in Figs. 10 and 14. The computed time series are

352   displayed for all the scenarios in Fig. 15 for the first 300 min of tsunami propagation.

353   If one considers the tide gauge offshore (node 1), the largest waves are due to the EHA

354   tsunami, that arrives in the shortest time and starts with an impulsive, positive, more than 1 m

355   amplitude, front. The first oscillation is strongly asymmetric and is followed by much weaker

356   waves, with dominant period of about 20 min. From the propagation pattern portrayed in Fig.

357   9, we know that this is the signal of the main front attacking Alexandria. The WHA tsunami is

358   second in size (about 1 m amplitude) and third in arrival time (about 40 min later). This is

359   consistent with the propagation snapshots shown in Fig. 5, where we can appreciate the arrival

360   of a very weak negative front at about 60-70 minutes after the earthquake occurrence, followed

361   by a much stronger positive front at 80-90 minutes. Large amplitude oscillations are observed

362   also after 140, 200 and 250 min. The CA signal arrives 5 minutes after the EHA tsunami and is

363   significantly weaker, and all the following oscillations are irregular and of similar amplitude.

364   Fig. 13 indicates that this is the signature of the western side of the tsunami front that is refracted

365   and loses energy while advancing towards the coast that here in the region of El Alamein, west

366   of Alexandria, has an overall concave shape.

367   Looking at tide gauge 2, one observes that the ranking of the scenarios as regards the

368   size and the arrival time is unchanged. Waves are remarkably amplified by a factor of 2 or more.

369   Tide gauge 4 is the last virtual sensor facing the open sea: here EHA and WHA exhibit

370   comparable maximum amplitudes, although at different arrival times. Moreover, EHA signal

371   amplitude is reduced with respect to tide gauge 2, while comparable values are observed for

372   WHA in the two virtual sensors, a similar observation holding also for CA. The time histories

373   of tide gauge 3 show the protecting effect of the harbour jetties and the interaction of the harbour

374   with incoming waves of different wavelengths. The size of the EHA signal is smaller than for

375   coastal tide gauges 2 and 4. The signal, however, seems to be dominated by normal modes of

376   the harbour basins more than by the source signature: the oscillations persist with little decay

377   for a longer time and seem to be "more periodic" with period of about 30-35 min for all

378   scenarios. These harbour basins normal modes are even more evident in the time-history

379   relative to WHA: the amplitude is comparable to those observed in tide gauges 2 and 4, and

380   remains almost unchanged for more than four hours.

381   A further consideration is that the arrival times of tsunamis at the coastal tide gauges are

382   in the order of 70-80 min and, in case of early warning, would allow exposed people to react

383   and to evacuate, provided that evacuation plans are implemented.

384

385   **The Aggregate Scenario**

386   Building the aggregate scenario is the last step of the scenario-based tsunami hazard

387   analysis. After selecting the appropriate tsunami metrics or parameters, one produces the

388   aggregate fields by taking the envelope of the individual scenarios, which more precisely means

389   by selecting the extreme of the values of the individual scenarios for each point of the field. In

390   this study a fundamental parameter is the depth of the water column in the inundated area that

391   has been shown in Figs. 6, 10 and 14 for the respective WHA, EHA and CA cases. The

392   corresponding envelope is shown in Fig. 16, which gives also the maximum inundation line

393   superimposed on a Google Earth image, marking the boundary between the area that is not

394   inundated by any one of the scenario tsunamis and areas that are inundated by at least one

395   tsunami. It has to be remarked that in practice the envelope is very similar to the EHA scenario,

396   with the exception of the Dekhila port area, where WHA gives the predominant contribution.

397   The identification of a single scenario with the aggregate one is not surprising, though it is not

398   the rule, but usually one finds a dominant scenario contributing to the aggregate much more

399   than all the others (see Tonini et al. 2011 for the town of Catania; see also Table 3 in Sørensen

400   et al., 2012, where the deaggregated weight of the single scenarios is estimated for various

401   towns in the Mediterranean).

402   Of interest is also the field of the maximum value of the speed of the material fluid

403   particles, whose aggregate is depicted in Fig. 17. Notice that in this example the portrayed field

404   is restricted to the still sea region and does not extend into the flooded area on land. Expectedly,

405   the velocity is small offshore where the water is deeper, and increases in the shallow water

406   region near the shore. The zones of the highest speed values, exceeding 3 m/s, include the tip

407   of the breakwaters and the narrow mouths of the harbours, especially in the Eastern and Western

408   Ports of Alexandria.

409

410   **Exposure and Vulnerability**

411   Exposure and vulnerability to tsunamis are concepts often used, but rarely well defined

412   in tsunami studies, in spite of the abundant literature on tsunami hazard, vulnerability, risk and

413 resilience that has been particularly flourishing after the megatsunamis of December 2004 in

414 the Indian Ocean and of March 2011 in Japan. Indeed, in spite of attempts to systematize the

415 conceptual framework, often researchers use the same terms for different concepts or different

416 words for the same concept (see the discussion on different approaches made by Birkmann and

417 Fernando 2008; see also Camarasa Belmonte et al. 2011). It is not in the scope of this paper to

418 provide a critical review of the subject, but for the sake of clarity it is relevant to highlight the

419 main concepts we use in our application. In this paper, the vulnerability of an element (or asset)

420 to tsunami is related to its capacity or ability to resist to the tsunami impact and depends on the

421 properties of the element. Usually one considers two broad categories of elements (the physical

422 inanimate objects, like buildings, cars, vessels, boulders, and the animate beings, like animals

423 and persons), that can be taken individually or in groups (e.g. complex of buildings, marinas

424 with boats and yachts, coastal forests, cultivated lands, passengers of ferries, tourists at the

425 beaches,…), and that can be also assembled at a higher level of complexity (examples of

426 vulnerable elements that can be placed at the top of complexity hierarchy are ecosystems, social

427 communities like villages and towns,…). The more complex is the element under study, the

428 more difficult is to measure its capacity of resisting to the attack of a tsunami and, consequently,

429 the harder is to provide properties and criteria to measure its vulnerability. And it is exactly in

430 the attempt of coping with a wide range of complexities that often researchers mix concepts

431 and place undefined boundaries between hazard, exposure, vulnerability, risk, resilience, etc.

432   In this paper, we will confine our attention only to the vulnerability of buildings, and

433 we will leave the assessment of vulnerability of more complex elements to further analyses. As

434 for the tsunami exposure, we simply consider that an element is exposed to a tsunami if it is

435 found in an area that can be reached by the tsunami. Therefore, elements that are in the sea, like

436 vessels and offshore structures are exposed, while elements that are on land, like edifices or

437 persons are exposed if their positions fall within the inundation area, and not exposed if they

438 happen to be outside the inundation area. This simple definition identifies the exposure with the

439 geographical position of the elements, that of course can be static (for a building), or variable

440 in time (for persons who might be on a beach susceptible of flooding in the day, and in a house

441 far away from the sea in the night). Since the extension of the flooded area depends on the

442 analyzed tsunami scenario, as was shown in the previous sections where the WHA, the EHA

443 and the CA tsunamis were investigated, accordingly also the number of elements exposed varies

444 from case to case.

445   In the frame of the above definitions, the goals of our work are to assess the vulnerability

446   of buildings that are found inside the inundation area of the aggregate scenario (shown in Fig.

447   16) and to estimate the number of persons that are exposed to tsunamis.

448

449   **Buildings Vulnerability Assessment**

450   Tsunami vulnerability is still a new science and has basically derived its chief analysis

451   tools from earthquake and flood vulnerability sciences that have a much longer tradition. The

452   main idea is that the vulnerability of an asset is described by means of damage functions. A

453   damage function puts in relation one or more hydrological parameters of the tsunami with the

454   damage level of the asset and can be inferred from empirical data (i.e. post-event field surveys

455   or laboratory experiments), from numerical simulations (e.g. theoretical studies of the structural

456   effects of tsunami waves and currents), and by means of heuristic analyses, or through a

457   combination of these methods. Though it is known that tsunami loading on buildings is exerted

458   via a number of various hydraulic forces (hydrostatic, surge, impact, buoyancy, etc.) that act in

459   combination, in most studies the tsunami parameters taken into account are the height of the

460   water column and less often the horizontal velocity of the flow and the momentum flux (that is

461   the product of the column water height by the squared velocity). Unfortunately, the speed of

462   the tsunami stream is quite difficult to determine for real tsunamis in the flooding areas and was

463   measured only in exceptional cases (see Fritz et al. 2012). Instead, the height of the tsunami

464   and tsunami run-up are standard observables of the tsunami post-event surveys. There is no

465   surprise, therefore, that most of the damage functions in the literature are based on the height

466   of the water column, also known as the flow depth (see Ruangrassamee et al. 2006; Koshimura

467   et al. 2009a and 2009b; Suppasri et al. 2013).

468   In this paper we make use of damage functions that are specific for different categories

469   of buildings based on the work by Leone et al. (2011) on the Indian Ocean tsunami, who

470   identified classes and subclasses of buildings mainly on the ground of their structural materials

471   and characteristics. These classes were revisited and adapted to the Euro-Mediterranean

472   building stocks in the European project SCHEMA, where also the original damage functions

473   were reappraised and modified (Valencia et al. 2011; Gardi et al. 2011). The five main buildings

474   classes from A to E considered in this paper are briefly summarized in Table 3 in a version

475   where all references to the buildings position is removed, since, according to our definition

476   given above, the geographical position of any asset pertains to the asset exposure rather than to

477   the asset vulnerability. For each buildings class Valencia et al. (2011) defined six levels of

478   damage from D0 (no damage) to D5 (total collapse), and, as a first stage, determined the

479   corresponding fragility curves, providing the probability that a building of that class might incur

480   in a damage Dj (j=0,1,…,5) as a function of the maximum flow depth. In the second stage, from

481   the fragility curves, they determined the damage functions, providing the maximum damage Dj

482   expected for a building of a given class as a function of the maximum flow depth. A synoptic

483   view of these curves is summarized in the damage matrix of Table 4 where each column

484   represents the discrete version of a damage curve for a specific buildings class. Note that the

485   damage matrix used in this study and presented in Table 4 is a modified version of the original

486   table by Valencia et al. (2011). In that formulation, a single damage level ("light damage") was

487   attributed to any building affected by a flow depth in the interval 0-1.8 m. The field observations

488   carried out for recent events like the 2011 Tohoku tsunami evidenced that this assumption is

489   not appropriate, as described and discussed for instance by Suppasri et al. (2013). In that work,

490   tsunami damage analyses performed on about 250,000 buildings after the Tohoku event showed

491   that for an inundation depth of 1 m to 1.5 m, more than 10% collapsed and about 55% suffered

492   major damages. To account for this variability, we modify classes A, B and C in Table 4: in

493   particular, with respect to Valencia et al. (2011) class A is completely redefined, class B is

494   modified for levels D0-D4 and class C for levels D0-D1. The modifications we propose derive

495   from the fragility curves reported in Reese et al. (2007) on the basis of the damage observed

496   after the 17 July 2006 Java tsunami.

497   The matrix provides a tool that is very simple and easy to implement: if one knows the

498   maximum flow depth attacking a building of a specific class, the matrix renders the maximum

499   expected incurring damage (see e.g. the applications by Atillah et al. 2011, Ribeiro et al. 2011

500   in the frame of the project SCHEMA).

501

502   **Buildings Damage Analysis**

503   The aggregate inundation area is portrayed in Fig. 16 on a Google Earth image

504   embracing all the coast of Alexandria from Al-Amriyah and El-Agami to Al-Montazah. It

505   shows that in all the coastline to the north-east of the old town, extending from Al-Gomrok to

506   Al-Montazah (see toponyms in Fig. 1) where most of the modern residential Alexandria has

507   been built, the inundation is limited only to beaches, since the coastal ridge is high enough to

508   oppose to the tsunami waves. On the contrary, the inundation in the zone from the Eastern Port

509   to Al-Amriyah and El-Agami is more severe and in some areas penetrates deep in the interior.

510   All the three harbours here (the Eastern and Western Ports and the Dekhila Port) are inundated,

511   which may be better appreciated in the zoom of Fig. 18. In the Eastern and Western Ports,

512   inundation affects the breakwaters and the former island of Pharos, that is the docking area for

513   cruise ships, as well as the area of Ras El Tin Palace and the Ras El Tin beach. In the Dekhila

514   Port, where the main activity is loading/unloading of cargos, the sea water goes about 2-3 km

515   far from the sea line, flooding the container terminal and deposits, silos, tanks… The area

516   suffering the major inundation is found in Wassat, around Al Max, where there is no protection

517   from the outer breakwater and where two flooding tongues penetrate 4 km deep (see Fig. 18)

518   following topographical lows corresponding to the drainage channels of the Lake Maryut. Here

519   the flooded area is occupied by big industrial plants and installations (e.g. the Solvay Alexandria

520   Sodium Carbonate company that is the main producer of soda ash for the domestic Egyptian

521   market; the Titan Cement company, a multinational company based in Greece that incorporated

522   the most important Egyptian cement producers in 2008; the Alexandria Petroleum Company

523   refinery), whereas the Al Max residential quarters are located at a level high enough to be almost

524   untouched.

525   To the south-west of Dekhila the inundation is very strong and involves further

526   installations of the Alexandria Petroleum Company refinery to the west, and a vast residential

527   area in Abu Talat and in El-Agami (Fig. 16). Since in this paper our main interest is in the

528   assessment of damage to buildings, we concentrate our analysis on this area. Indeed, the damage

529   matrix of Table 4 is inadequate for industrial installations and infrastructures, that should be

530   rather analyzed by means of specific studies, since in this case not only the direct effects are of

531   importance, but the induced cascade effects might be even more relevant and worth of a

532   thorough investigation (see the disaster following the meltdown of three reactors of the

533   Fukushima Daiichi nuclear power plant induced by the Japan 2011 tsunami; see also Cruz et al.

534   2011). Therefore, we leave this subject for further studies.

535   The buildings damage analysis in the area to the south-west of the Dekhila port is

536   essentially based on images of the Google Earth database, including satellite imagery and

537   ground pictures. Since the beginning of vulnerability assessment science, remote sensing with

538   global coverage has been seen as a powerful and practical tool to conduct vulnerability studies

539   over vast coastal areas. It is worth stressing that from the experience gained in very many

540   applications it has been shown that, though in principle ground surveying is necessary to

validate remote sensing based analyses, often it results only in slight corrections, and a few control points may suffice for a good validation (see Tonini et al. 2011, and Pagnoni et al. 2014 for buildings vulnerability studies on eastern Sicily towns).

In this paper the buildings damage analysis has been performed according to the following 5 step procedure.

• First, the area of inundation resulting from the envelope scenario with 40 m resolution is put in a Google Earth file format. This allows one to import the inundation area in the Google Earth satellite images, as displayed in Figs. 16 and 18 already referred to above. Here it is worth stressing that the need to superimpose the computed inundation area to georeferenced Google Earth images derives from the fact that the potential tsunami damage is estimated by cross-checking data of tsunami inundation (available in maps produced by the tsunami simulation code UBO-TSUFD) with data on the buildings, inferable from the Google Earth satellite most recent images (acquired on January, 20 2015 and on April, 18 2015). It is further worth underlining that such images are quite recent in the Alexandria region, since they were mostly acquired in years 2014 and 2015.

• Step 2 consists in the land use characterization of the flooded area with the purpose of identifying the zones with buildings where to focus vulnerability and damage analysis. This enabled us to restrict the analysis to the zone to the south-west of the Dekhila port illustrated in green in Fig. 19 and to discard other sectors of the aggregate flooded area because either they are industrial zones (APC refinery) or container terminals (Dekhila port) (see the red zones of Fig. 19) or they are basically with no buildings (e.g. beaches, swamps…).

• Step 3 is the creation of a discretization grid suitable for both flow depth analysis and buildings vulnerability analysis. When no automatic digital tool for image processing is available and when the extension of the inundation area is large, painstaking visual inspection can be a very heavy and time-consuming process, with costs increasing with the grid resolution. In our study we have considered as useful compromise a 80 m resolution tessellation, by which we have covered the part of the inundation area resulting from the selection of step 2. Fig. 20 portrays the flow depth (water column height) of the envelope scenario for the 80 m grid, that is easily built from the 40 m grid of the tsunami numerical model by proper node selection, since by purpose the size of the tessellation grid cell is a multiple of the simulation grid. This is an advantage but is not a strict requirement, since all normal interpolation methods are

572 straightforward and adequate to compute coarser fields from higher resolution maps. From the

573 flow depth map (Fig. 20) one can observe that the highest values are in the range of 3-4 m and

574 that are mostly found close to the shoreline. Expectedly the flow depth decreases moving

575 landward, but there are two remarkable high zones with values between 2-3 m (red in the

576 Figure) that can be explained as the effect of local topographic lows.

577 • In step 4, by making use of the adopted tessellation, we identify all the buildings that

578 are located within the selected portion of the inundation area and assign each of them to one of

579 the five buildings classes from A to E given in Table 3. Figure 21 provides Google Earth

580 pictures of buildings typical of each class. The analysis is performed for each cell of the

581 tessellation. We have counted a total of 2433 inundated cells, covering an area of about 15.571

582 km^2. At this stage, a more accurate inspection showed that as many as 479 cells (around 20%

583 of the total) have no buildings: most of these are located on the coast and cover the area between

584 the coastline and the first line of buildings (see Figure 22 displaying the map of the building

585 density per cell). It is worth observing that in attributing the building to a given cell, buildings

586 on the cell boundary are counted in the cell if their footprint is inside the cell in a proportion

587 larger than 50%, which entails some degree of overestimation, with a bias that is larger in

588 percentage, the smaller the cell size is. On the other hand, when deducing the flow depth in

589 each cell (which is done in step 3), the bias decreases along with the cell size. This explains that

590 a further requirement of the step 3 tessellation (in our case 80 m) has to be a compromise

591 between the counting of buildings (with estimate improving with the size of the cells) and the

592 assumption that the value of the inundation depth is constant within a cell (with approximation

593 worsening with the cell size). The total number of constructions within the flooded zone has

594 been found to exceed 12,000. Most of them are brick houses with some reinforced structural

595 elements (class D), or mere brick houses (class C) or more solid buildings with reinforced

596 concrete (class E), and only a few are weak brick houses (class B) or light constructions (class

597 A). The distribution of buildings into the adopted SCHEMA classes is shown in Table 5. The

598 number of buildings per cell, that can also be seen as a building density, is shown through the

599 histogram of Figure 23 and the map of Figure 22. To help readability, all classes of Figure 23

600 have width 2 and are denoted on the horizontal axis with an even number. This means that a

601 generic class denoted by 2n contains all tessellation cells counting either 2n-1 or 2n buildings.

602 The first class is an exception: it has width 1 since it contains only cells with 0 buildings. Of

603 the 2433 (80 m x 80 m) cells, as many as 479 result to be with no constructions, as already

604   noted before. Considering only the occupied cells, one observes that the highest columns of the

605   histograms are the classes ranging from 3 to 8 buildings. Further, the average density results to

606   be 5.1 bpc (here bpc stands for buildings per cell) and, if one restricts only to the occupied cells,

607   it increases to about 6.3 bpc. The building density map (<mark>Fig. 22</mark>) shows that no-building cells

608   are found i) along the shoreline, ii) in alignments normal to the shore, corresponding to stream

609   banks, and iii) in areas close to the industrial (on the left) and port (on the right) installations.

610   •   The fifth step of our procedure is the evaluation of the damage that might incur to each

611   building by applying the modified damage matrix shown in Table 4. The result of the analysis

612   is summarized in Table 6. The first four columns give respectively the flow depth discretized

613   in steps consistent with the damage matrix, the corresponding number of cells, the area they

614   cover, and the overall number of buildings they contain. From the table, one sees that the

615   number of cells, and therefore the corresponding area, decreases strongly as the flow depth

616   increases. The area where the sea level is found to be less than 1 m results to be as much as

617   59% of the total, while only 5.8 % is inundated by more than 2.5 m of sea water. Consequently,

618   also the number of affected buildings (column 4 of the table) is an inverse function of the flow

619   depth. It is worth noting that the building density in the least inundated cells turns out to be 5.56

620   bpc which is somewhat larger than the average (5.1 bpc). Notice further that this density tends

621   to decrease as the flow depth increases: it is 4.0 bpc for the central flow-depth class (1.5-2 m)

622   well below the average, and goes down to the extreme value of 0.95 bpc for the most inundated

623   cells. This shows that the areas subject to the highest tsunami inundation (usually found close

624   to the shoreline or the river banks) have been traditionally considered by local people not

625   adequate for population settlements. Determining if this has occurred as the result of specific

626   tsunami hazard awareness or of more generic flooding hazard awareness or of other reasons

627   related to construction technique (inadequacy of soil for foundation) is out of the scope of the

628   present analysis. However it is a noteworthy feature since it has a positive consequence on

629   reducing the potential tsunami damage.

630   The other columns of Table 6 display the frequency distribution of the damage level

631   from D0 to D5. Notice that since by choice all the considered buildings are found inside the

632   inundation area, none of them falls in the D0 damage category, that applies only to buildings

633   not affected by any tsunami wave. The sub-table including the columns from D1 to D5 can be

634   commented by considering rows, i.e. the flow depth, or by considering columns, i.e. the damage

635   level. In the first case, one may notice that when the flow depth is small (less than 1.0 m) all

21

636   buildings incur only damage D1, with the exception of less than 0.2% of constructions incurring

637   in damage of type D2. With higher values of flow depth, the distribution of buildings tend to

638   be less peaked, involving also other levels of damage, and at the highest flow depth values, i.e.

639   between 3.5-4 m, some buildings are found to incur in the maximum level of damage, D5. The

640   final result of this analysis is that 11732 buildings are expected to have a damage not exceeding

641   D1 (light), as many as 479 a damage not exceeding D2 (important), 143 a heavy damage (D3)

642   and only 39 and 5 buildings can be affected respectively by partial collapse (D4) and total

643   collapse (D5).

644   The buildings damage estimates summarized in Table 6 are the result of the 5-step

645   procedure illustrated above where at some point we have introduced a convenient 80-m

646   resolution tessellation in place of the 40 m grid resulting from the tsunami simulations. In doing

647   so we have assumed that the flow depth of the envelope scenario is constant in each cell of the

648   tessellation and have taken this constant value, say d, to assess the damage to all constructions

649   inside the cell, with account for their respective vulnerability class. It is trivial to see that the

650   tessellation cell spans an area covered by 4 tsunami grid cells, in general with different flow

651   depth values. If we denote respectively the highest and smallest of such values with d_{max} and

652   d_{min}, and repeat the damage assessment by making use of these values, we will obtain

653   respectively higher and lower damage levels for the buildings in the cell. Table 7 gives the total

654   number of buildings in each damage class resulting from applying the analysis in all cells of

655   the inundation area. Comparing Table 7 with the last row of Table 6, one sees that figures

656   computed with the flow d are bracketed by the ones obtained by using d_{max} and d_{min}, which

657   provides an estimate of the uncertainties deriving from the coarser discretization of the

658   tessellation grid. In our case, the general pictures of the damage analyses of Table 6 and Table

659   7 do not differ substantially, and therefore the 80 m resolution can be considered acceptable in

660   this respect.

661   The vulnerability analysis illustrated here is the result of the careful identification of the

662   building types that are located in each single cell of the tessellation, which is a manual procedure

663   taking long if one extends the analysis to the full set of the tessellation cells, as was done before.

664   One could wonder how the final results are affected if one takes into consideration only a

665   suitable selected cells sample. To this purpose we have selected a number of random samples,

666   each of 243 cells, thus corresponding to the 10% of the total tessellation set. The results are

667   shown and discussed in the Appendix A1.

Population Exposure Analysis

668

669 **Population Exposure Analysis**

670   The population exposure is computed from census data of Alexandria. Since we are

671 considering a residential area, we assume that there is no seasonal variability, which is usually

672 related to touristic fluxes. Further, we neglect also the daily variability assuming that all

673 residents are at home, which is consistent with the worst-case scenario approach adopted in this

674 study.

675   Census in Egypt is conducted regularly every 10 years since 1976 and there are data for

676 the years 1937, 1947 and 1960. The last survey was carried out in 2006 by the Central Agency

677 for Public Mobilization and Statistics (CAPMAS). The census data provided by CAPMAS

678 regard mainly constructions and population. As to the former, one can trace the huge expansion

679 of the building patrimony for the whole Egypt as well as for the individual governorates. The

680 increase of the number of buildings for the governorate of Alexandria is shown in the histogram

681 plotted in Fig. 24 for the interval 1944-2015 where the data of the national surveys are

682 interpolated and extrapolated for those years not covered by the surveys. One can observe a

683 more than 10 times increase in the last 55 years with building stock passing from 31.3 thousand

684 to about 390 thousand in 2015.

685   The population of Egypt has a general growing trend with an increase of more than 22%

686 in the years from 1996 and 2006, which is rather homogeneous throughout the country. In the

687 same decade, the governorate of Alexandria population grew by 20% passing from 4 million to

688 4.8 million people while in the last 55 years the population grew by a factor slightly less than

689 3.3 (see the histogram of Fig. 25). By combining census data on buildings and population, one

690 can draw the curve of the people density per buildings as a function of time, which is also

691 provided in Figure 25. One can see that this density went remarkably and steadily down from

692 69.5 to about 11.6 ppb (persons per building) in the second half of the 20th century, and that it

693 started to increase slowly after the 2000, reaching the value of 12.4 ppb in 2015. This people

694 density is the basic figure that allows us to estimate the persons resident within the aggregate

695 inundation area shown in Fig. 20. The last column of Table 6 gives the number of exposed

696 persons that are resident in areas with different estimated level of flow depth, where the figures

697 are obtained simply by multiplying the corresponding number of buildings listed in column 4

698 by the average density factor of 12.4. The total number of exposed people results to be 153916,

699 which is quite large in absolute value, though it is only 3.2% of the total population of the

23

700 governorate. We stress that the population density we have used is the average value for the

701 governorate of Alexandria evaluated for the year 2015 and that using values specific for the

702 districts where the inundation area extends could provide more accurate, but expectedly not so

703 different, estimates.

704

705 **Comparison with other studies**

706 The tsunami vulnerability of Alexandria has been the subject of only one previous paper,

707 to the knowledge of the authors. On making use of remote sensing and field data, Eckert at al.

708 (2012) estimated the building vulnerability of Alexandria by applying a vulnerability model

709 that is based on flow depth values, but also on several other attributes of the buildings. Since

710 three basic factors of Eckert et al. study (i.e. usage of remote sensing data, usage of field data,

711 damage functions taking into account flow depth values) are common with the present paper

712 analysis, one could expect similarities in the result, which is unfortunately not true. The two

713 studies happen to be incomparable and totally inconsistent in the conclusions, since the hazard

714 analysis, that is a prerequisite for the vulnerability analysis is quite different. Adopting a

715 bathtub-like approach and skipping numerical modelling, Eckert et al. (2012) investigated two

716 tsunami scenarios where the sea level rises by 5 m and by 9 m uniformly all along the coast of

717 Alexandria due to a tsunami attack. Since under this hypothesis the inundation area covers the

718 entire coast of the governorate of Alexandria, for practical reasons they restricted the analysis

719 to the districts of Al-Gomrok and Al-Montazah (see Fig. 1 for toponyms). However, according

720 to our study based on worst-case credible scenarios, the buildings in these two districts result

721 to be almost untouched by the tsunami, since the inundated area turns out to be more to the

722 south-west, and even here run-up values do not reach 10 m height.

723

724 **Conclusions**

725 In this paper we have investigated the tsunami hazard of Alexandria by using the

726 WCTSA technique. We have considered three scenarios (WHA, EHA and CA) where tsunamis

727 are generated by big earthquakes in the subduction arcs marking the boundary between the

728 Africa and the Eurasia plates. All these are remote sources, which means that seismic shaking

729 is expected to be moderate in Alexandria and that tsunami is the major threat. We have

730 considered two possible level for the sea, the mean sea level and the maximum high-tide level,

24

731 that are assumed to differ by 30 cm in Alexandria, in agreement with tide-gauge time-series

732 analysis.

733   The inundation resulting from enveloping the inundation maps of the individual cases

734 happen to be very similar to (although not coincident) the EHA scenario, that is therefore the

735 predominant one; the WHA scenario adds a relevant contribution especially in the El Dekhila

736 area. Flooding affects mostly the Alexandria coast to the west of the old town where a number

737 of tongues (two in the area between Al-Gomrok and El Dekhila and two more to the south west

738 of El Dekhila) penetrates some kilometres on land beyond the coastal ridge, primarily exploiting

739 the drainage channels of the Lake Maryut. We have applied a buildings vulnerability model

740 elaborated in the European project SCHEMA to estimate the damage to buildings in the affected

741 residential areas of El Dekhila and Al-Amriyah. In case of tsunami simulations in mean-sea-

742 level conditions, our finding is that 12398 constructions can be damaged (most of which only

743 slightly) by the tsunami and that about 154000 residents are exposed, which corresponds to the

744 3.2% of the total population of the governorate of Alexandria. These figures increase to 13340

745 for buildings and to 165,308 for persons, when tsunami simulations are carried out for the

746 maximum high-tide level conditions.

747   The present study can be considered preliminary and will be refined in future work. One

748 key point is the hazard analysis that should investigate not only earthquake sources but all the

749 possible credible large tsunami sources. In our discussion on tsunami hazard for Alexandria we

750 have mentioned a Holocene huge mass flow whose tsunamigenic potential was investigated by

751 Garziglia et al. (2007). We believe that it would be interesting to explore whether small scale

752 submarine sediment movements are able to generate tsunami affecting Alexandria more severely

753 than the earthquake-induced tsunamis, and hence to contribute to the aggregate scenario. Further,

754 uniform-slip earthquake sources have been assumed here, while it is well known that for all large

755 earthquakes the on-fault co-seismic slip occurs in patches with the slip magnitude much higher than

756 the average value. Third, as regards vulnerability analysis, we remark that the damage to buildings

757 might be only a fraction of the total economic loss especially when the hit area is full of large

758 industrial plants with high pollution potential like the ones in the analyzed districts of Alexandria.

759 In addition, these industries act as attraction points for workers, which increases the number of

760 persons exposed to tsunami especially during day light. This is also true for the port structures that

761 are key port terminals for the whole Egypt country. Deepening these topics is at the frontier of the

762 today's tsunami vulnerability analysis and will be subject of future research.

770

771   **Appendix A1**

772   Counting the buildings in all the cells of the area resulting from the envelope of tsunami

773   inundation maps can be a very long procedure, taking time resources increasing with the

774   extension of the area, which can cover tens or hundreds of km^2. In the case of Alexandria studied

775   here, the inundation area covers more than 15 km^2 and involves 2433, 80 m x 80 m, cells and

776   12398 constructions. In order to reduce the time for the analysis, one might consider to apply

777   the vulnerability analysis to a subset of such cells, under the assumption that results are

778   representative of the entire set. We have investigated this possibility by taking as many as 10

779   samples of the 2433 cells, each consisting of 243 cells (about 10% of the total). Each sample

780   resulted from a random selection (corresponding from sampling a uniform distribution of

781   integers running from 1 to 2433), tempered however by the criterion that the selected cells

782   should be distributed almost uniformly over the entire inundation area. This latter requirement

783   was checked by visual inspection and was used to avoid concentration of cells in specific

784   geographic zones with properties far from the ensemble properties (e.g. with very low or very

785   high buildings density, or with very low or very high flow depth, etc.).

786   To each of the 10 samples we have applied the procedure described in the paper section

787   on vulnerability analysis, and then estimated the values for the entire set. In particular, we have

788   counted the number of buildings for each building type from A to E and the total number of

789   buildings of the sample. It is easy to see that if N_S is one of these numbers, the statistical standard

790   deviation associated to it is $\sigma_S = \sqrt{N_S}$, and the estimates of the corresponding number for the

791   entire set are αN_S and $\alpha \sigma_S$ where α is the ratio between the total number of cells and the number

792   of cells in the sample. In our case $\alpha = 10$. The results are shown in Fig. A1 where for each

793   building types the estimates are provided together with the error bars. They are compared with

the corresponding values we obtained by using the full set of data shown in Table 6. It can be observed that for most samples the real values (solid black lines) are within the 1-σ error bar (exception are samples 2, 5 and 6) and that for all samples they fall within the 1.5 σ error bar.

If we extend the analysis from the above building classification to the damage evaluation, we obtain a similar plot (see Fig. A2). The number of buildings with a given level of damage obtained by the samples usually falls within 1σ error bar, and always within the 1.5 σ error bar. This proves that making estimates on samples can be a viable tool to obtain satisfactory results and to save analysis time, though, however, the cost to pay is to introduce same statistical error.

Appendix A2

In Alexandria, like in most of the Mediterranean sea, sea level oscillations due to tides are much less relevant than in the oceans. A ten-year long record (1996-2005) of daily sea level oscillations taken in the Western Port of Alexandria shows that tidal range is confined to about 60 cm (see El-Geziry and Radwan, 2012), of which about 18 cm are due to the astronomical tide contribution and the rest to surges. On the basis of these data, we have assumed that the maximum high-tide level is 30 cm above the mean sea level and, accordingly, we have changed the local topo-bathymetry of the grid 4, that is the one covering Alexandria with the highest resolution (40 m), and performed tsunami simulations for all the relevant earthquake sources. Following the same analysis procedure used in the paper, we have first assembled the aggregate, then computed the inundation area and made estimates on the involved buildings and people.

Expectedly, the aggregate inundation area increases passing from 15.6 km^2 to 16.4 km^2, which in terms of tessellation cells, constructions and persons leads to the respective totals of 2560 (vs. 2433), 13340 (vs. 12398) e 165,608 (vs. 153,916). There are 942 more buildings falling in the more extended inundation area most of which (72%) happen to belong to least vulnerable classes D and E. Table A2.1 shows the new buildings class distribution. The maximum high-tide sea level condition entails a higher water column in all inundated cells. Comparing Table A2.2 with the analogous Table 6, one sees that the number of cells with water height in the 3-4 m range almost doubles (increasing from 37 to 71) and that also cells in the ranges 1-2 m and 2-3 m increase respectively from 675 to 739, and from 292 to 356. Likewise, also the damage level to buildings gets higher. From Table A2.3 where the frequency distribution of buildings damage level is shown for the mean-sea-level as well as the maximum

27

high-tide level aggregate inundation, one can observe that the highest increment is found for the light damage level D1. It may also be noted that the frequency of buildings with the most severe damage level (D5 = total collapse) increases by a factor larger than 2 (from 5 to 11). Eventually, after applying the same estimation algorithm used in the main text, we are able to pass from the number of involved buildings to the evaluated number of exposed residents portrayed in the last column of Table A2.2. They are as many as 165,608. Of these, about 109,500 live in zones with inundation depth less than 1 m, but about 11000 can be in serious trouble since they reside in low-land areas, where the inundation depth may exceed 2 m. Looking at Table 6, where the corresponding estimates calculated for the mean-sea-level conditions are displayed, one sees that about 108,000 people live in areas with less than 1 m inundation and that about 7000 live where tsunami inundation can be higher than 2 m. It's worth noting that the increment of the number of exposed people is not proportionally distributed among the discrete classes of inundation height, but conversely the number of people living in cells with expected higher water level increases (both in percentage and in absolute value) much more than the number of people in low inundation level.

References

842 Altinok, Y. and Ersoy, S.: Tsunamis observed on and near the Turkish Coast, Nat. Hazards, 21,
843

844 185–205, 2000.

845 Altinok, Y., Alpar, B., Ozer, N., and Aykurt, H.: Revision of the tsunami catalogue affecting

846 Turkish coasts and surrounding regions, Nat. Hazards Earth Syst. Sci., 11, 273–291, 2011.

847 Ambraseys, N.N.: Data for the investigation of the seismic seawaves in the Eastern

848 Mediterranean, Bull. Seismol. Soc. Am., 52, 895–913, 1962.

849 Ambraseys, N.N., Melville, C.P., and Adam, R.D.: The Seismicity of Egypt, Arabia and the

850 Red Sea: A Historical Review, Cambridge University Press, Cambridge, UK, 1994.

851 Atillah, A., El Hadani, D., Moudni, H., Lesne, O., Renou, C., Mangin, A., and Rouffi, F.:

852 Tsunami vulnerability and damage assessment in the coastal area of Rabat and Sale,

853 Morocco, Nat. Hazards Earth Syst. Sci., 11, 3397–3414, 2011.

854 Antonopoulos, J. A.: Data from the investigation of seismic sea-wave events in the eastern

855 Mediterranean from the birth of Christ to 1980 AD (six parts), Ann. Geophys., 33, 141–

856 248, 1980, http://www.ann-geophys.net/33/141/1980/.

857 Birkmann, J. and Fernando, N.: Measuring revealed and emergent vulnerabilities of coastal

858 communities to tsunami in Sri Lanka, Disasters, 32, 82-105, 2008.

859 Brizuela, B., Armigliato, A., and Tinti, S.: Assessment of tsunami hazard for the American

860 Pacific coast from southern Mexico to northern Peru, Hazards Earth Syst. Sci., 14:1889-

861 1903, 2014.

862 Burbidge, D., Cummins, P.R., Mleczko, R., and Thio, H.A.: Probabilistic tsunami hazard

863 assessment for Western Australia, Pure Appl. Geophys., 165, 2059–2088, 2008.

864 Camarasa Belmonte, A.M., López-García, M.J., and Soriano-García, J.: Mapping temporally-

865 variable exposure to flooding in small Mediterranean basins using land-use indicators,

866 Appl. Geogr., 31, 136-145, 2011.

867 Cruz, A.M., Krausmann, E., and Franchello, G.: Analysis of tsunami impact scenarios at an oil

868 refinery, Nat. Hazards, 58, 141-162, 2011.

869 Ebeling, C.W., Okal, E.A., Kalligeris, N., and Synolakis, C.E.: Modern seismological

870 reassessment and tsunami simulation of historical Hellenic Arc earthquakes,

871 Tectonophysics, 530–531, 225–239, 2012.

872 Eckert, S., Jelinek, R., Zeug, G., and Krausmann, E.: Remote sensing-based assessment of

873 tsunami vulnerability and risk in Alexandria, Egypt, Appl. Geogr., 32,714-723, 2012.

874   El Alami, S.O. and Tinti, S.: A preliminary evaluation of the tsunami hazards in the Moroccan

875   coasts, Science of Tsunami Hazards, 9, 31-38, 1991.

876   El-Geziry, T.M., Abd Ellah, R.G., and Maiyza, I.A.: Bathymetric Chart of Alexandria Eastern

877   Harbor, Egyptian J. Aquatic Res., 33, 15-21, 2007.

878   El-Geziry, T.M. and Radwan, A.: Sea level analysis off Alexandria, Egypt, Egyptian J. Aquatic

879   Res., 38, 1-5, 2012.

880   El-Sayed, A., Romanelli, F., and Panza, G.: Recent seismicity and realistic waveforms

881   modeling to reduce the ambiguities about the 1303 seismic activity in Egypt,

882   Tectonophysics, 328, 341–357, 2000.

883   Fokaefs, A. and Papadopoulos, G.A.: Tsunami hazard in the Eastern Mediterranean: strong

884   earthquakes and tsunamis in Cyprus and the Levantine Sea, Nat. Hazards, 40, 503–526,

885   2007.

886   Fritz, H.M., Phillips, D.A., Okayasu, A., Shimozono, T., Liu, H.J., Mohammed, F., Skanavis,

887   V., Synolakis, C.E., and Takahashi, T.: The 2011 Japan tsunami current velocity

888   measurements from survivor videos at Kesennuma Bay using LiDAR, Geophys. Res.

889   Lett., 39, L00G23, doi: 10.1029/2011GL050686, 2012.

890   Gardi, A., Valencia, N., Guillande, R., and André, C.: Inventory of uncertainties associated with

891   the process of tsunami damage assessment on buildings (SCHEMA FP6 EC co-funded

892   project), Nat. Hazards Earth Syst. Sci., 11, 883-893, 2011.

893   Garziglia, S., Ioualalen, M., Migeon, S., Ducassou, E., Mascle, J., Sardou, O., and Brosolo, L.:

894   Triggering Factors and Tsunamigenic Potential of a Large Submarine Mass Failure on

895   the Western Nile Margin (Rosetta Area, Egypt), in: Lykousis, V., Sakellariou, D., Locat,

896   J. (Eds.), Submarine Mass Movements and Their Consequences - Advances in Natural

897   and Technological Hazards Research, Springer, Dordrecht, The Netherlands, 27, 347-

898   355, 2007.

899   Geist, E.L. and Parsons, T.: Probabilistic analysis of tsunami hazards, Nat. Hazards 37, 277–

900   314, 2006.

901   Grilli, S.T., Taylor, O.D.S., Baxter, C.D.P., and Maretzki, S.: Probabilistic approach for

902   determining submarine landslide tsunami hazard along the upper East Coast of the United

903   States, Mar. Geol., 264, 74-97, 2009.

904   Grilli, S.T., Harris, J., and Tajalli Bakhsh, T..: Literature Review of Tsunami Sources Affecting
905   Tsunami Hazard Along the US East Coast, NTHMP Progress report, Res. Rept. CACR-
906   11-08, Center for Applied Coastal Research, University of Delaware, Newark, 2011.

907   Gonzalez, F.I., Geist, E.L., Jaffe, B., Kanoglu, U., Mofjeld, H., Synolakis, C.E., Titov, V.V.,
908   Arcas, D., Bellomo, D., Carlton, D., Horning, T., Johnson, J., Newman, J., Parsons, T.,
909   Peters, R., Peterson, C., Priest, G., Venturato, A., Weber, J., Wong, F., and Yalciner, A.:
910   Probabilistic tsunami hazard assessment at Seaside, Oregon, for near- and far-field
911   seismic sources, J. Geophys. Res., 114, C11023, doi:10.1029/2008JC005132, 2009.

912   Guidoboni, E., Comastri, A., and Traina, G.: Catalogue of Ancient Earthquakes in the
913   Mediterranean Area up to 10th Century, Istituto Nazionale di Geofisica, Roma, 1994.

914   Guidoboni, E. and Comastri, A.: The large earthquake of 8 August 1303 in Crete: seismic
915   scenario and tsunami in the Mediterranean area, J. Seismol., 1, 55–72, 1997.

916   Guidoboni, E. and Comastri, A.: Catalogue of Earthquakes and Tsunamis in the Mediterranean
917   area from the 11th to the 15th Century, INGV-SGA, Bologna, 2005.

918   Koshimura, S., Namegaya, Y., and Yanagisawa, H.: Tsunami Fragility: a new measure to assess
919   tsunami damage, J. Disaster Res., 4, 479–488, 2009a.

920   Koshimura, S., Oie, T., Yanagisawa, H., and Imamura, F.: Developing fragility curves for
921   tsunami damage estimation using numerical model and post-tsunami data from Banda
922   Aceh, Indonesia, Coast Eng. J., 51, 243–273, 2009b.

923   Leonard, L.J., Rogers, G.C., and Mazzotti, S.: Tsunami hazard assessment of Canada, Nat.
924   Hazards, 70, 237-274, 2014.

925   Leone, F., Lavigne, F., Paris, R., Denain, J.C., and Vinet, F.: A spatial analysis of the December
926   26th, 2004 tsunami-induced damages: lessons learned for a better risk assessment
927   integrating buildings vulnerability, Appl. Geogr. 31, 363–375, 2011.

928   Lin, I.C. and Tung, C.C.: A preliminary investigation of tsunami hazard, Bull.. Seismol. Soc.
929   Am., 72, 2323–2337, 1982.

930   Lorito, S., Selva, J., Basili, R., Romano, F., Tiberti, M.M., and Piatanesi, A.: Probabilistic
931   Hazard for Seismically-Induced Tsunamis: Accuracy and Feasibility of Inundation Maps,
932   Geophys. J. Int., 200, 574-588, 2015.

933   Lorito, S., Tiberti, M.M., Basili, R., Piatanesi, A., and Valensise, G.: Earthquake-generated
934   tsunamis in the Mediterranean Sea: Scenarios of potential threats to Southern Italy, J.
935   Geophys. Res., 113, B01301, doi:10.1029/2007JB004943, 2008.

936 Okada, Y.: Internal deformation due to shear and tensile faults in a half-space, Bull. Seismol.
937   Soc. Am., 82, 1018-1040, 1992.

938 Pagnoni, G., Tinti, S., and Rallo, F.: Application and comparison of tsunami vulnerability
939   models in the gulf of Siracusa, Sicily, EGU General Assembly, Vienna, Austria, 27 April
940   – 2 May 2014, EGU2014-10621, 2014.

941 Papadopoulos, G.A.: A Seismic History of Crete: Earthquakes and Tsunamis, 2000 B.C. – A.D.
942   2010, Ocelotos Publications, Athens, 2011.

943 Papadopoulos, G.A., Daskalaki, E., Fokaefs, A., and Giraleas, N.: Tsunami hazards in the
944   Eastern Mediterranean: strong earthquakes and tsunamis in the East Hellenic Arc and
945   Trench system, Nat. Hazards Earth Syst. Sci., 7, 57–64, 2007.

946 Papadopoulos, G.A., Gràcia, E., Urgeles, R., Sallares, V., De Martini, P.M., Pantosti, D.,
947   González, M., Yalciner, A., Mascle, J., Sakellariou, D., Salamon, A., Tinti, S.,
948   Karastathis, V., Fokaefs, A., Camerlenghi, A., Novikova, T., and Papageorgiou, A.:
949   Historic and pre-historic tsunamis in the Mediterranean and its connected seas:
950   documentation, geological signatures, generation mechanisms and coastal impacts, Mar.
951   Geol., 354, 81-109, 2014.

952 Pararas-Carayannis, G.: The Earthquake and Tsunami of July 21, 365 in the Eastern
953   Mediterranean Sea - Review of Impact on the Ancient World - Assessment of Recurrence
954   and Future Impact, Science of Tsunami Hazards, 30, 253-292, 2011.

955 Pirazzoli, P.A., Ausseil-Badie, J., Giresse, P., Hadjidaki, E., and Arnold, M.: Historical
956   environmental changes at Phalasarna harbor, West Crete, Geoarchaeology, 7, 371–392,
957   1992.

958 Pirazzoli, P.A., Laborel, J., and Stiros, S.C.: Earthquake clustering in the eastern Mediterranean
959   during historical times, J. Geophys. Res., 101, 6083-6097, 1996.

960 Reese, S., Cousins, W.J., Power, W.L., Palmer, N.G., Tejakusuma, I.G., and Nugrahadi, S.:
961   Tsunami vulnerability of buildings and people in south Java – field observations after the
962   July 2006 Java tsunami, Nat. Hazards Earth Syst. Sci., 7, 573-589, 2007.

963 Ribeiro, J., Silva, A., and Leitão, P.: High resolution tsunami modelling for the evaluation of
964   potential risk areas in Setúbal (Portugal), Nat. Hazards Earth Syst. Sci., 11, 2371–2380,
965   2011.

966 Ruangrassamee, A., Yanagisawa, H., Foytong, P., Lukkunaprasit, P., Koshimura, S., and
967   Imamura, F.: Investigation of Tsunami-induced damage and fragility of buildings in

Thailand after the December 2004 Indian Ocean Tsunami, Earthq. Spectra, 22, 377–401, 2006.

Salamon, A., Rockwell, T., Ward, S.N., Guidoboni, E., and Comastri, A.: Tsunami Hazard Evaluation of the Eastern Mediterranean: Historical Analysis and Selected Modeling, Bull. Seismol. Soc. Am., 97, 705–724. doi:10.1785/0120060147, 2007.

Shaw, B., Ambraseys, N.N., England, P.C., Floyd, M.A., Gorman, G.J., Higham, T.F.G., Jackson, J.A., Nocquet, J.M., Pain, C.C., and Piggott, M.D.: Eastern Mediterranean tectonics and tsunami hazard inferred from the AD 365 earthquake, Nat. Geosci., 1, 268-276, 2008.

Soloviev, S.L., Solovieva, O.N., Go, C.N., Kim, K.S., and Shchetnikov, N.A.: Tsunamis in the Mediterranean Sea 2000 B.C. – 2000 A.D., Advances in natural and technological hazards research, 13, Kluwer Academic Publisher, Dordrecht, 2000.

Sørensen, M.B., Spada, M., Babeyko, A., Wiemer, S., and Grünthal, G.: Probabilistic tsunami hazard in the Mediterranean Sea, J. Geophys. Res., 117, B01305, doi:10.1029/2010JB008169, 2012.

Stiros, S.C.: The AD 365 Crete earthquake and possible seismic clustering during the 4–6th centuries AD in the Eastern Mediterranean: a review of historical and archaeological data, J. Struct. Geol., 23, 545–562, 2001.

Stiros, S.C.: The 8.5+ magnitude, AD 365 earthquake in Crete: Coastal uplift, topography changes, archaeological and historical signature, Quatern. Int., 216, 54-63, doi:10.1016/j.quaint.2009.05.005, 2010.

Suppasri, A., Mas, E., Charvet, I., Gunasekera, R., Imai, K., Fukutani, Y., Abe, Y., and Imamura, F.: Building damage characteristics based on surveyed data and fragility curves of the 2011 Great East Japan tsunami, Nat. Hazards, 66, 319–341, 2013.

Tinti, S.: Assessment of tsunami hazard in the Italian Seas, Nat. Hazards, 4, 267-283, 1991a.

Tinti, S.: Tsunami potential in Southern Italy, Science of Tsunami Hazards, 9, 5-14, 1991b.

Tinti, S., Armigliato, A., Pagnoni, G., and Zaniboni, F.: Scenarios of giant tsunamis of tectonic origin in the Mediterranean, ISET J. Earthq. Techn., 42, 171–188, 2005.

Tinti, S. and Tonini, R.: The tsunami inundation model UBO-TSUFD: Validation and application to a tsunami case study focused on the city of Catania, Italy, Nat. Hazards Earth Syst. Sci., 13, 1795-1816, 2013.

999 Tonini, R., Armigliato, A., Pagnoni, G., Zaniboni, F., and Tinti, S.: Tsunami hazard for the city
1000   of Catania, eastern Sicily, Italy, assessed by means of Worst-case Credible Tsunami
1001   Scenario Analysis (WCTSA), Nat. Hazards Earth Syst. Sci., 11, 1217-1232, 2011.

1002 Valencia, N., Gardi, A., Gauraz, A., Leone, F., and Guillande, R.: New tsunami damage
1003   functions developed in the framework of SCHEMA project: application to European-
1004   Mediterranean coasts, Nat. Hazards Earth Syst. Sci., 11, 2835-2846, 2011.

1005 Yolsal-Çevikbilen, S. and Taymaz, T.: Earthquake source parameters along the Hellenic
1006   subduction zone and numerical simulations of historical tsunamis in the Eastern
1007   Mediterranean. Tectonophysics, 536–537, 61–100, 2012.

1008
1009
1010

1011 **Table 1.** Fault parameters for the three scenarios analysed in the paper.

Fault	WHA	EHA	CA
Length (km)	130	100	100
Width (km)	86	46.7	46.7
Strike	314°	236°	280°
Dip	35°	20°	20°
Rake	90°	90°	90°
Slip (m)	17.5	8.0	8.0
Upper edge depth (km)	5	5	5

1012
1013

1014 **Table 2.** Topo-bathymetric datasets used to build grids 1 to 4 for tsunami simulations.

Name	Type	Resolution	Coordinate System
GEBCO	Raster topo-bathymetric	30 arcsec	Geographical
SRTM	Raster topographic	~90 m	Geographical
Digitized nautical chart	Bathymetric contour lines and scattered points	1:5000 1:10000	UTM
Digitized from El-Geziry et al. (2007)	Bathymetric contour lines and scattered points	~20 m	UTM
Google Earth Topography	Transects	Control points	Geographical

1015

1016

1017 **Table 3.** Buildings classes after the project SCHEMA (Valencia et al., 2011). Any reference
1018 to building exposure is removed.

Class		Building attributes	Storeys
I. Light constructions	**A1**	Very light isolated constructions. Wooden, timber, clay materials	0 to 1 level, rarely 2
	A2	Very light constructions without any design (like in a shantytown). A set of huts very rudimentary, built using wood, clay, timber, slabs of zinc	1 level only
	A3	Light constructions very concentrated (like in old towns). Wooden, timber and clay materials	1 level only
II. Masonry constructions & not reinforced concrete	**B**	Brick not reinforced. Cement, mortar walls, fieldstone, masonry	1 or 2 level
	C	Individual buildings, villas. Brick with reinforced column & masonry filling	1 or 2 level
	D	Large villas or collective buildings, residential or commercial buildings. Not reinforced concrete	1 to 3 level

35

Class		Building attributes	Storeys
III. Reinforced concrete constructions	**E1**	Residential or collective structures or offices, car parks, schools. Reinforced concrete, steel frame	0 to 3 levels
	E2	Residential or collective structures or offices, car parks, schools, towers. Reinforced concrete, steel frame	> 3 levels

Table 4. Building damage matrix after the project SCHEMA (Valencia et al., 2011) modified in buildings classes A and B following the fragility curves proposed by Reese (Reese et al., 2007). The first column reports the description of the damage level. The columns from A to E give the flow depth intervals in meters. Notice that damage D0 is attributed only to buildings reached by no tsunami waves.

Damage level		Class A	Class B	Class C	Class D	Class E
No damage	**D0**	0	0	0	0	0
Light damage	**D1**	0 – 0.5	0 – 1	0 – 2	0 – 2.8	0 – 3
Important damage	**D2**	0.5 – 1	1 – 2	2 – 4	2.8 – 4.5	3 – 6
Heavy damage	**D3**	1 – 2	2 – 4	4 – 6	4.5 – 6.5	6 – 9.5
Partial collapse	**D4**	2 – 3	4 – 5	6 – 8	6.5 – 9	9.5 – 12.5
Total collapse	**D5**	> 3	> 5	> 8	> 9	> 12.5

Table 5. Vulnerability classification of the buildings inside the aggregate inundation area selected in step 2 of the procedure. It extends for over 15 km^2. <mark>Data refer to the mean-sea-level case.</mark>

Vulnerability classification						
Class	**A**	**B**	**C**	**D**	**E**	**Tot**
Number of buildings	106	1092	3208	4123	3869	12398

Table 6. Damage to buildings and exposed persons under the hypothesis of mean-sea-level conditions.

Flow depth (m)	Number of cells	Area (km²)	Number of buildings	Number of buildings						Persons
				D0	D1	D2	D3	D4	D5	
0.0-0.5	744	4.76	4809	0	4809	0	0	0	0	59702
0.5-1.0	685	4.38	3881	0	3866	15	0	0	0	48181
1.0-1.5	395	2.53	2018	0	1808	189	21	0	0	25052
1.5-2.0	280	1.79	1118	0	972	123	23	0	0	13879
2.0-2.5	185	1.18	396	0	209	85	74	28	0	4916
2.5-3.0	107	0.68	141	0	68	40	22	11	0	1750
3.0-4.0	37	0.24	35	0	0	27	3	0	5	434
Total	**2433**	**15.57**	**12398**	**0**	**11732**	**479**	**143**	**39**	**5**	**153,916**

Table 7. Maximum and minimum number of buildings attributed to each level of damage. Notice that the number of buildings shown in the last row of Table 6 lies in between the ones of this table. Data computed for simulations made in case of mean-sea-level conditions.

	Number of buildings					
	D0	D1	D2	D3	D4	D5
d_{max}	0	11390	720	210	54	24
d_{min}	0	11950	351	87	10	0
Difference	**0**	**-560**	**+369**	**+123**	**+44**	**+24**

Table A2.1. Vulnerability classification of the buildings inside the aggregate inundation area under the assumption of maximum high-tide. It extends for over 16 km².

Vulnerability classification						
Class	**A**	**B**	**C**	**D**	**E**	**Tot**
N° buildings	109	1156	3407	4390	4278	13340

Table A2.2. Damage to buildings and exposed persons in case of maximum high-tide conditions.

Flow depth (m)	N° Cells	Area (km²)	N° Buildings	Number of buildings						Persons
				D0	D1	D2	D3	D4	D5	
0.0-0.5	700	4.48	4708	0	4708	0	0	0	0	58448
0.5-1.0	694	4.44	4106	0	4093	13	0	0	0	50974
1.0-1.5	444	2.84	2419	0	2173	224	22	0	0	30031
1.5-2.0	295	1.89	1224	0	1073	131	20	0	0	15195
2.0-2.5	224	1.43	622	0	364	130	97	31	0	7721
2.5-3.0	132	0.84	196	0	93	60	32	11	0	2433
3.0-4.0	71	0.45	65	0	0	47	7	0	11	806
Total	2560	16.38	13340	0	12504	605	178	42	11	165,608

Table A2.3. Number of buildings per level of damage in case of mean sea level (msl) and of maximum high-tide level (MHL).

Sea level	Number of buildings					
	D0	D1	D2	D3	D4	D5
msl	0	11732	479	143	39	5
MHL	0	12504	605	178	42	11
Difference (MHL - msl)	0	772	126	35	3	6

1059
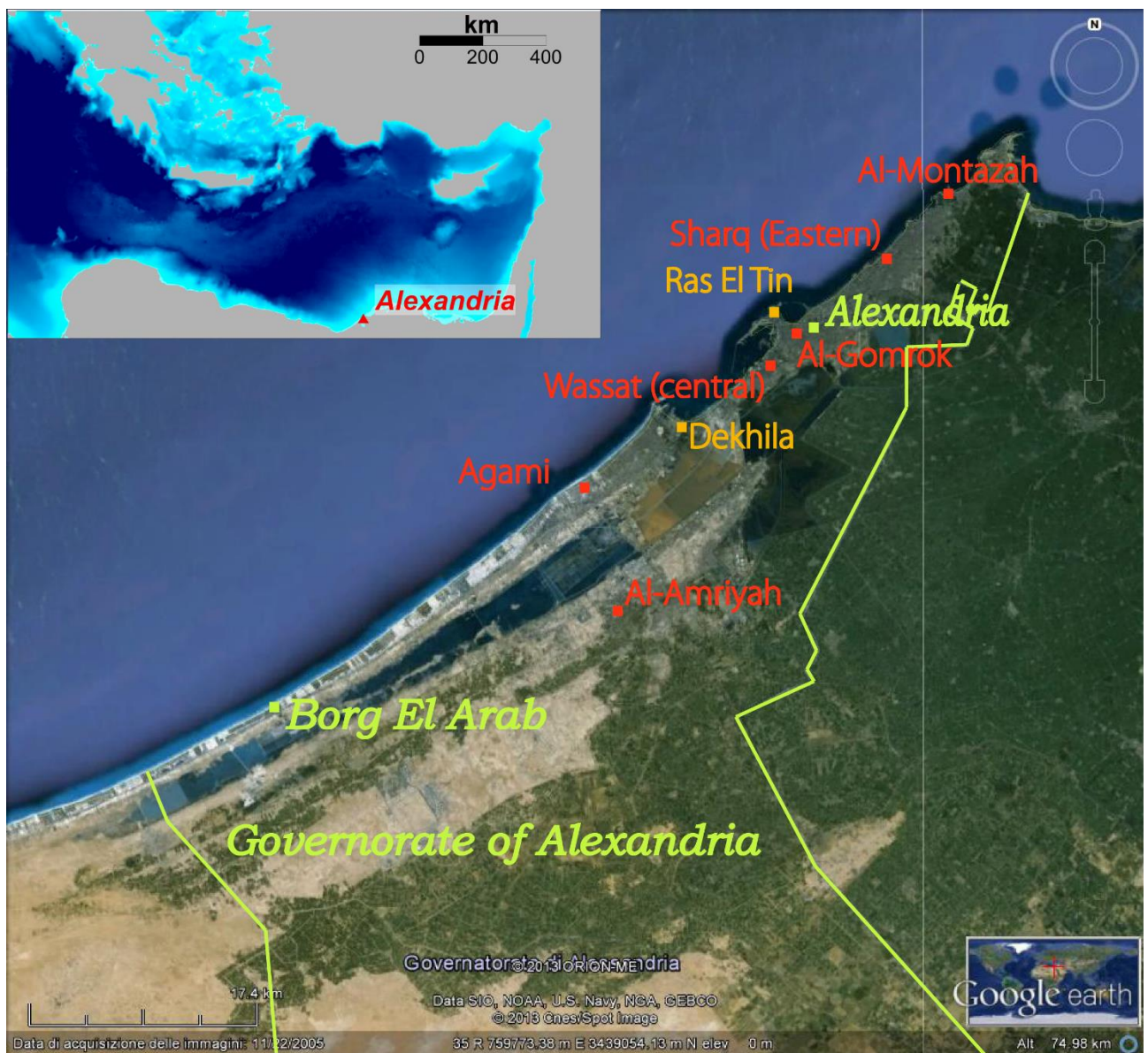
1060　Figure 1. Governorate of Alexandria. Names of the districts are in red. Places that result affected

1061　by major inundation according to the computations of the paper are in orange. In the upper left

1062　corner a map of the eastern Mediterranean including Alexandria.

1063
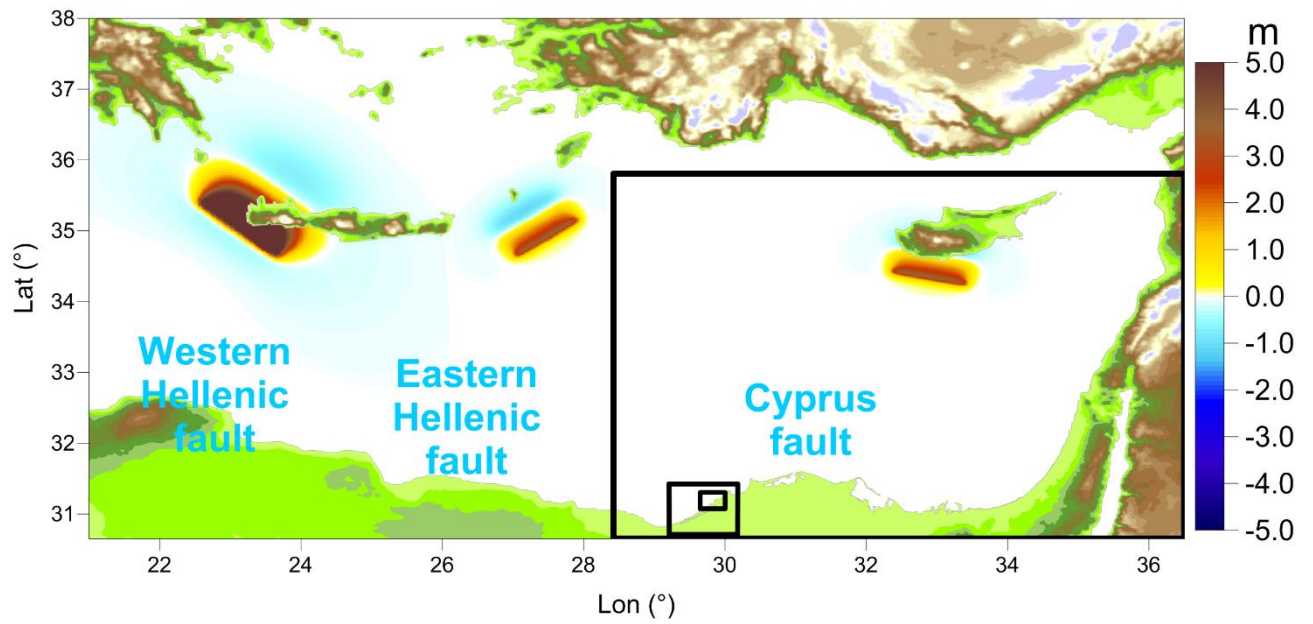
Figure 2. Initial sea surface elevation for the three tsunami scenarios treated in the paper. Tsunami simulations are carried out in four grids: the outer grid (grid 1) coincides with the map shown here, while the three black boxes show the boundaries of the three nested grids (grid 2 to 4). Grid 4, centered on Alexandria, has two different topo-bathymetric data: one for the mean-sea-level tsunami simulations and one for the maximum high-tide tsunami simulations, which differ by the uniform static value of 30 cm.
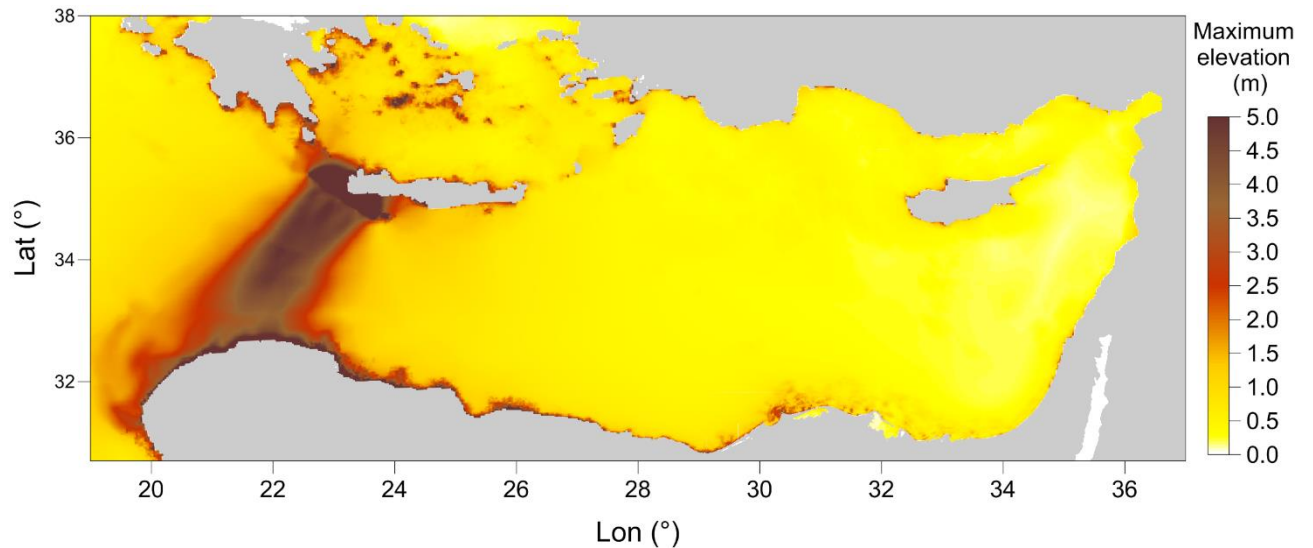
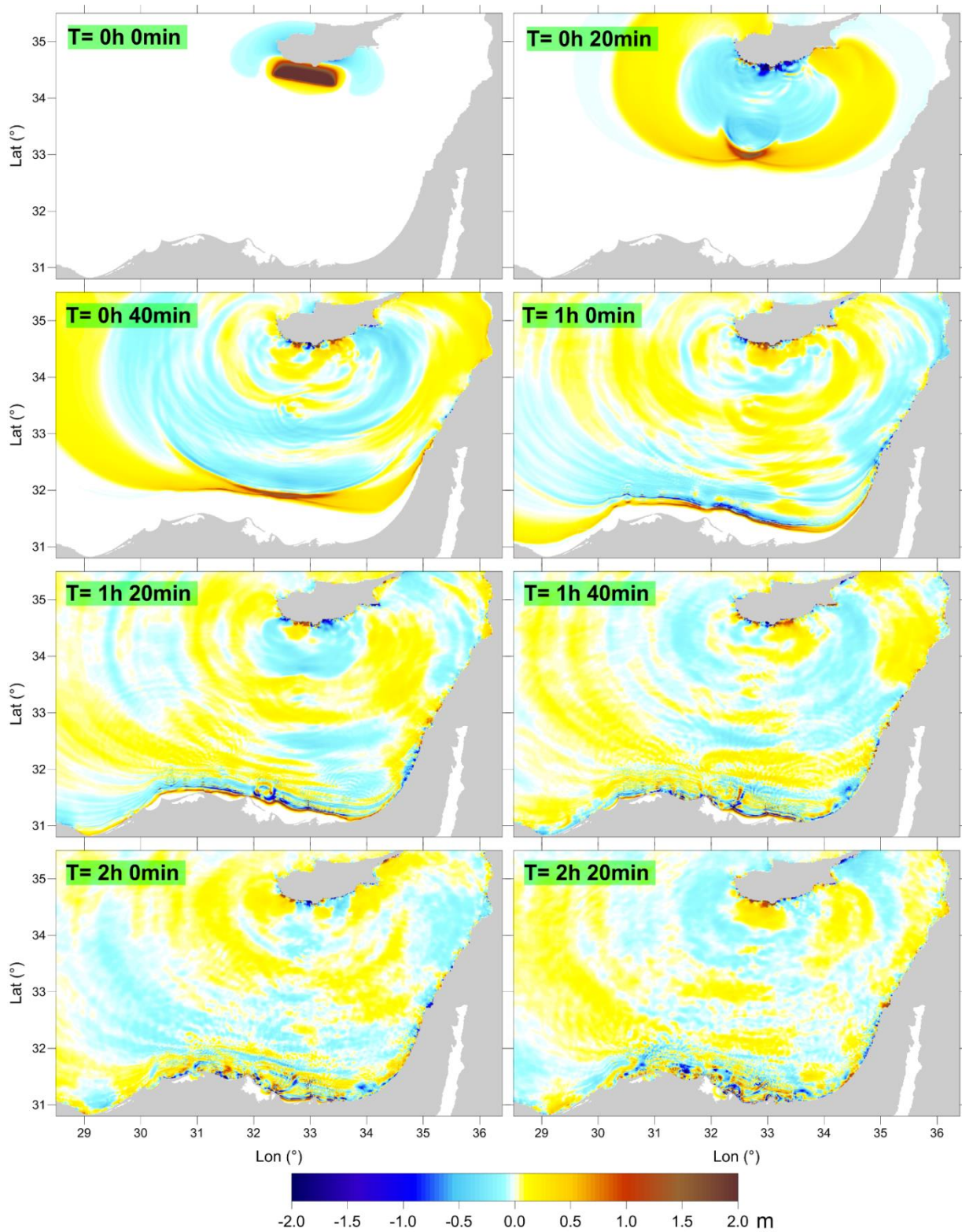Figure 3. Sea surface maxima in grid 1 for the tsunami generated by the Western Hellenic Arc (WHA) earthquake (see Table 1 for details).
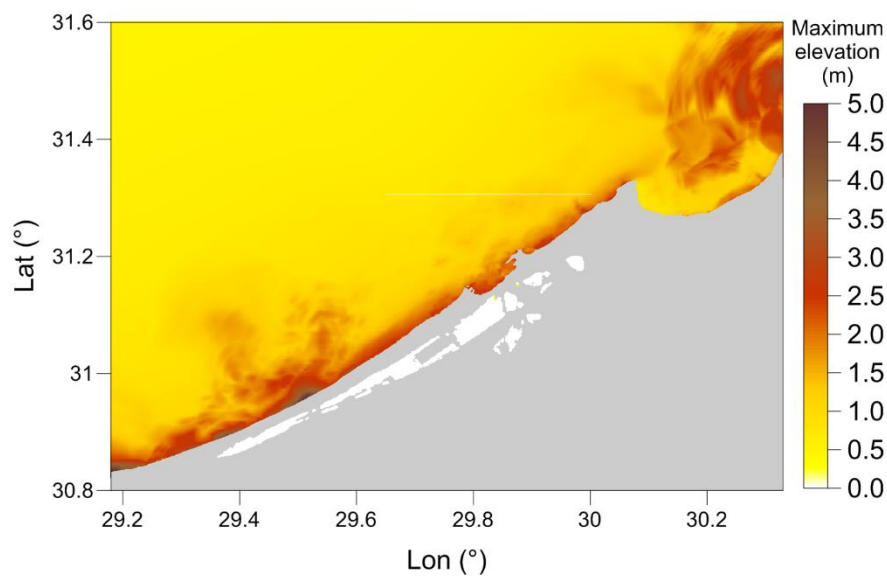
Figure 4. Sea surface maxima for the WHA source, zoomed in the area of Alexandria with grid 3 (200 m resolution).
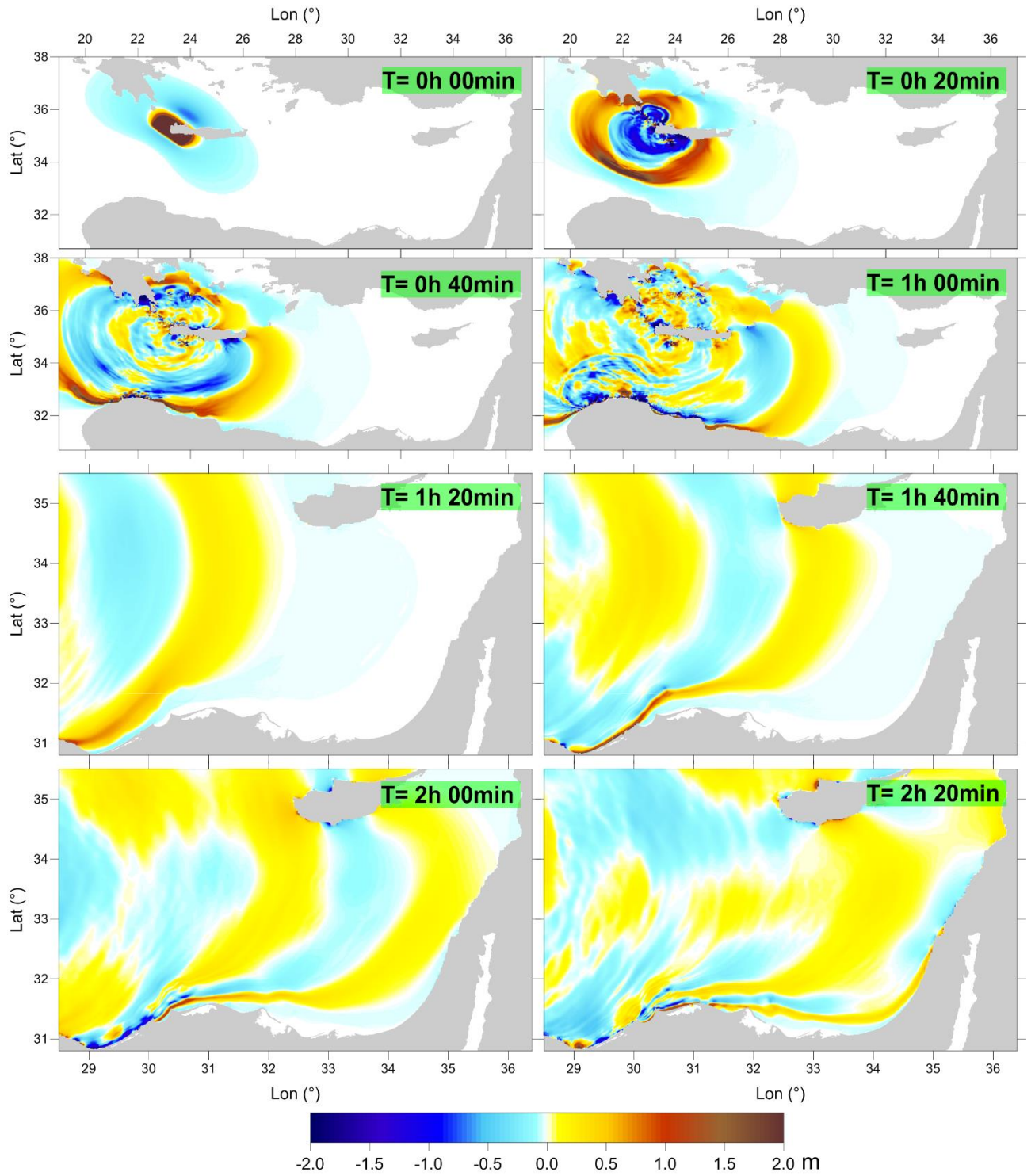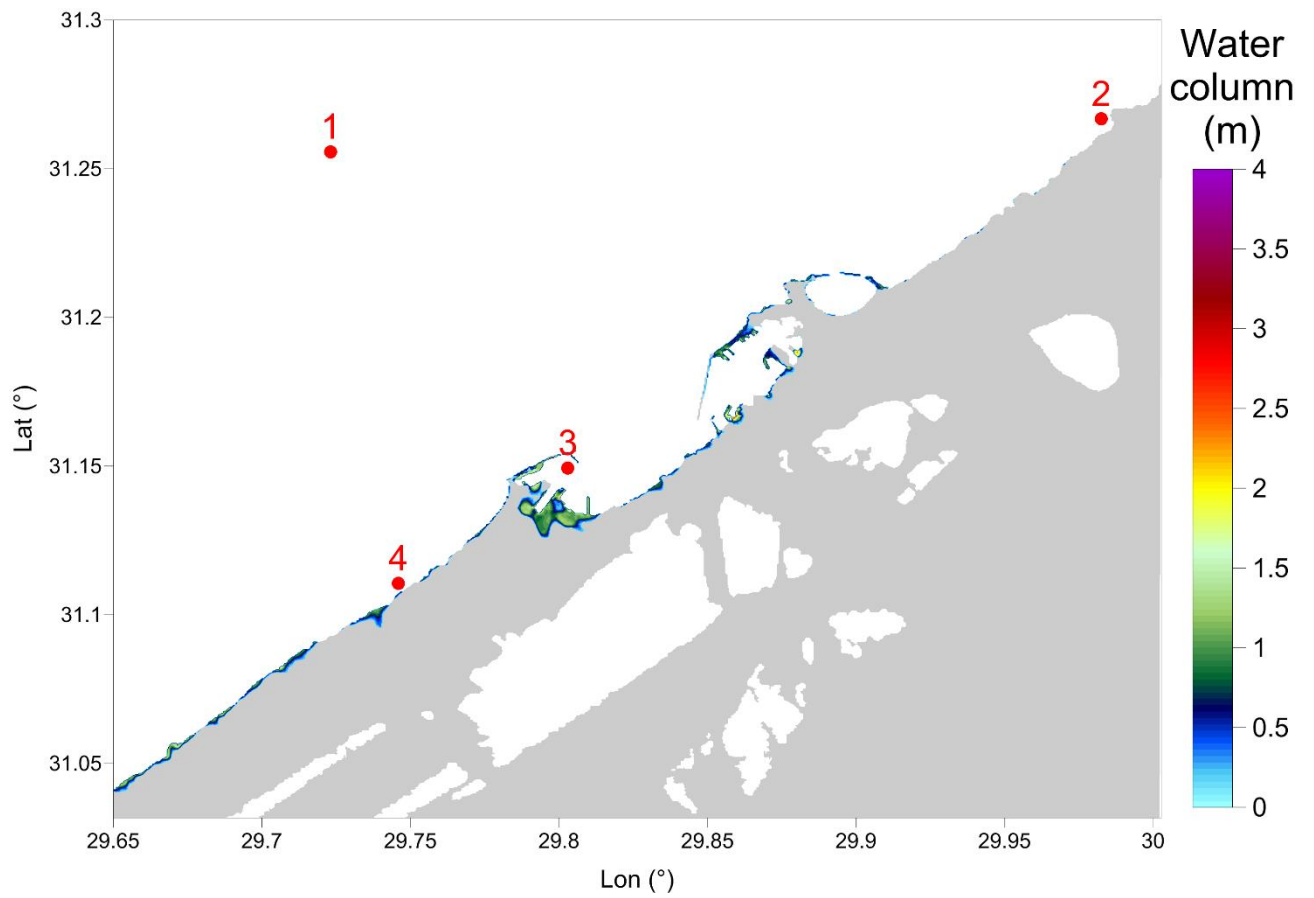
Figure 5. Propagation fields for the WHA tsunami scenario. Snapshots taken every 20 minutes. Fields from t=0 to t=1hr are plotted in grid 1, the other ones in grid 2.

1084
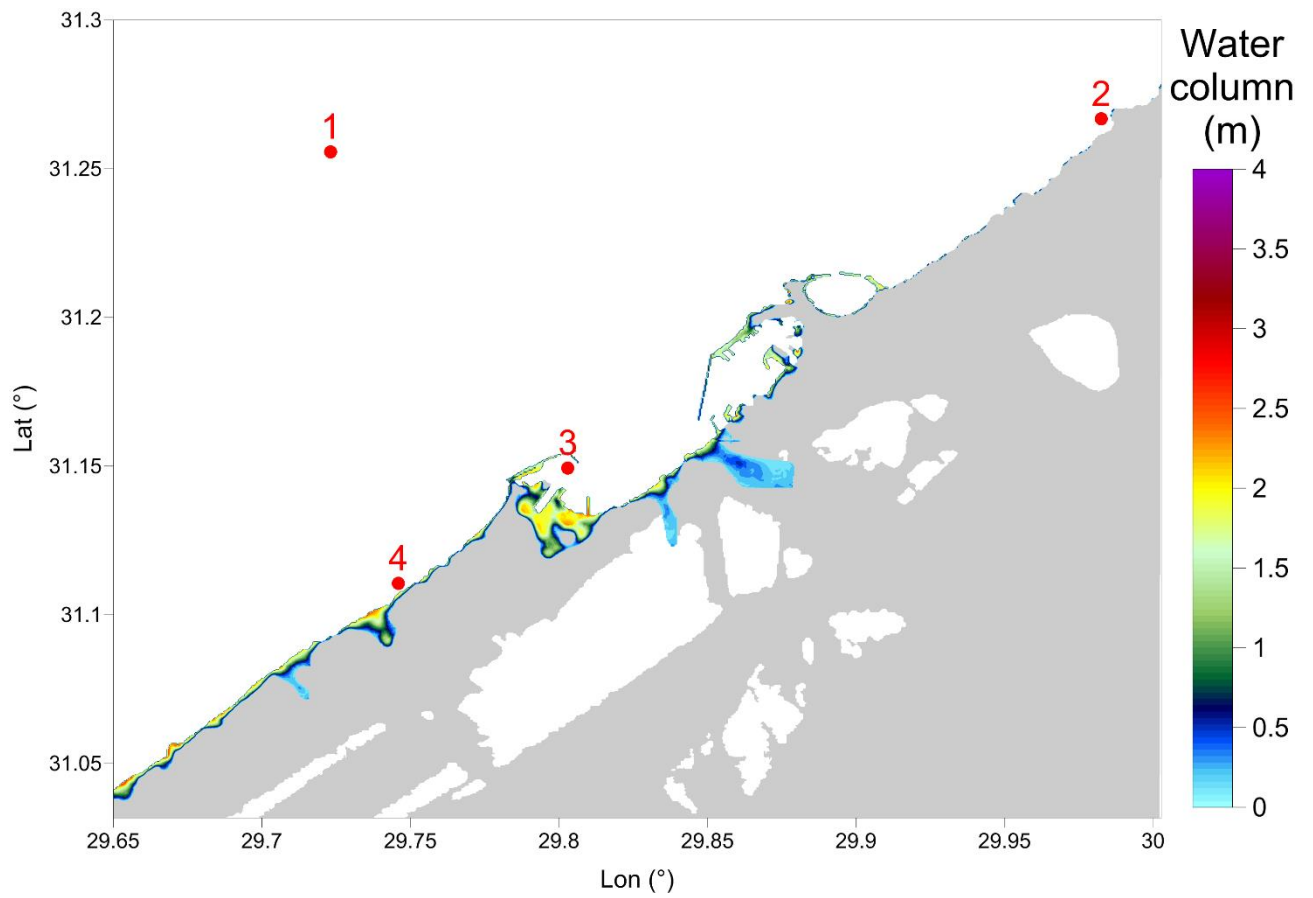
Figure 6. Water depth maxima on land for the WHA case plotted in grid 4 (40 m resolution) in mean-sea-level conditions. Red circles show the position of four virtual tide gauges: gauge 1 quite offshore, the others three very close to the coast.

1088

1089
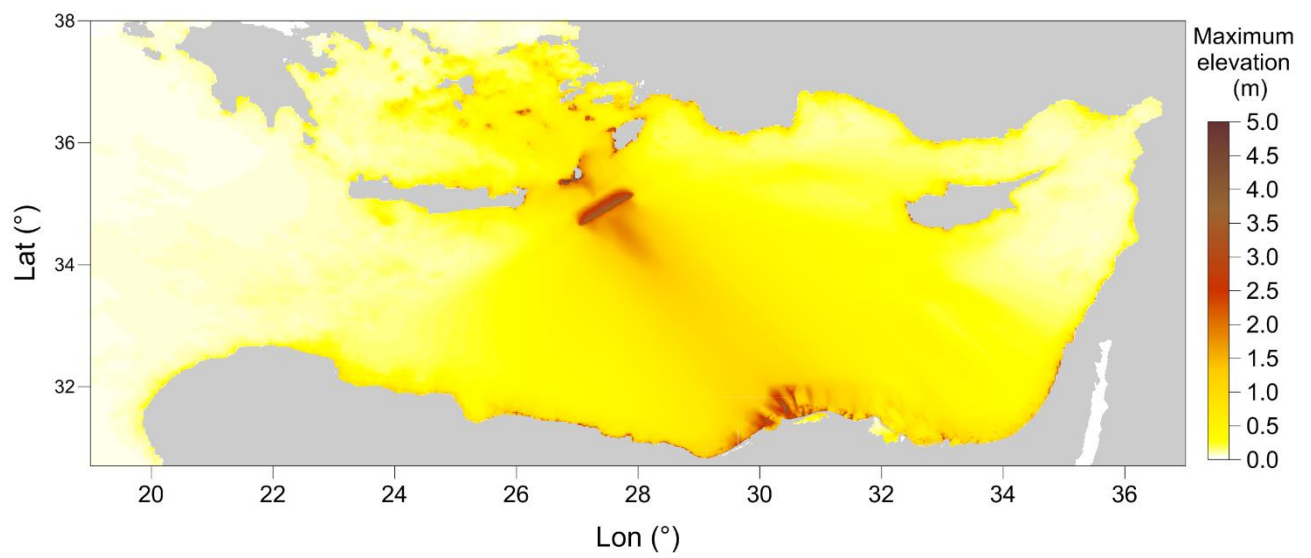
1090 Figure 7. Sea surface maxima in grid 1 for the tsunami generated by the Eastern Hellenic Arc

1091 (EHA) earthquake (see Table 1 for details).

1092

1093
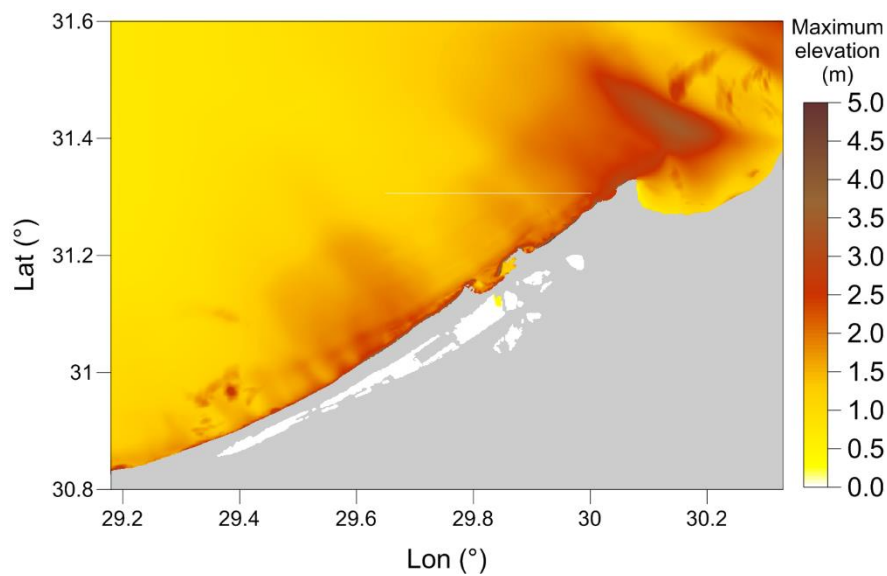
1094 Figure 8. Sea surface maxima for the EHA source, zoomed in the area of Alexandria with grid

1095 3 (200 m resolution).

1096

44

Figure 9. Propagation fields for the EHA tsunami scenario. Snapshots taken every 20 minutes. Fields from t=0 to t=20 min are plotted in grid 1, the other ones in grid 2.

1100
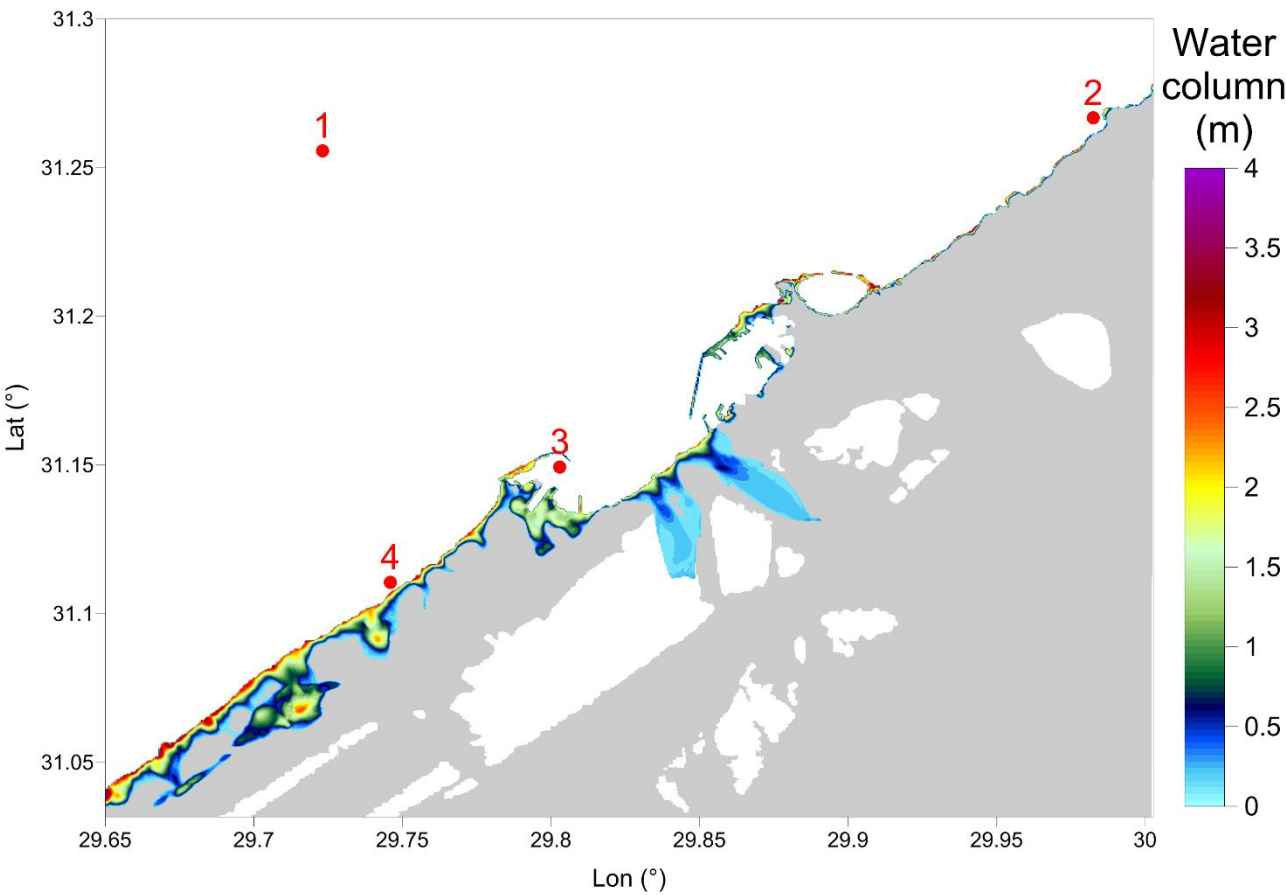
1101

1102 Figure 10. Water depth maxima on land for the EHA case plotted in grid 4 (40 m resolution) in
1103 mean-sea-level conditions. See caption of Fig. 6 for further details.

1104

1105
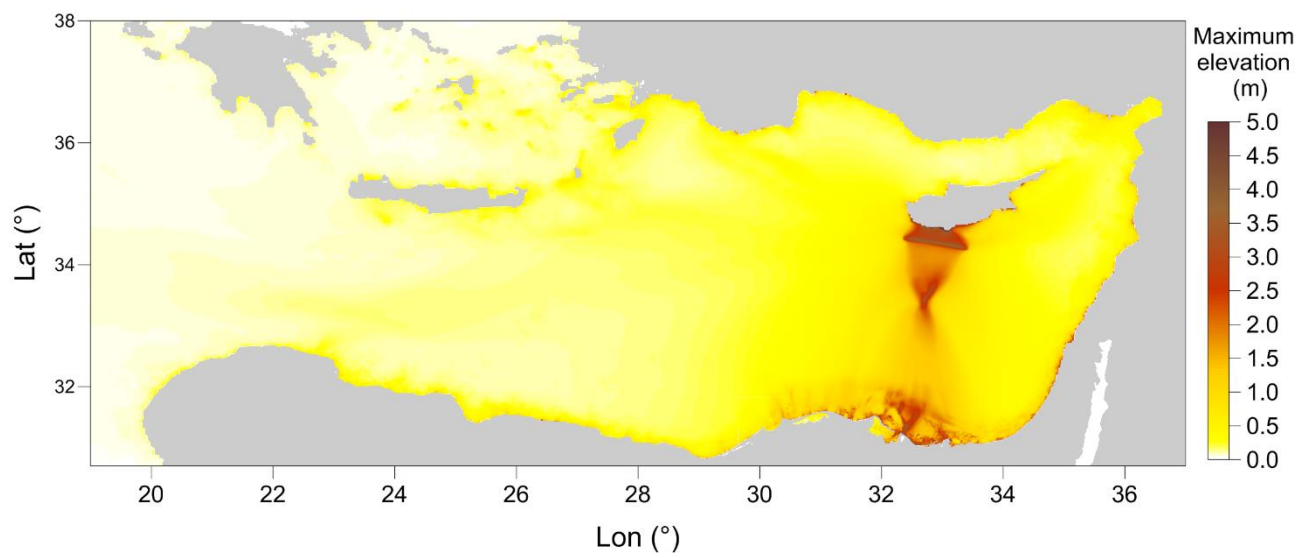
1106 Figure 11. Sea surface maxima in grid 1 for the tsunami generated by the Cyprus Arc (CA)

1107 earthquake (see Table 1 for details).

1108

1109
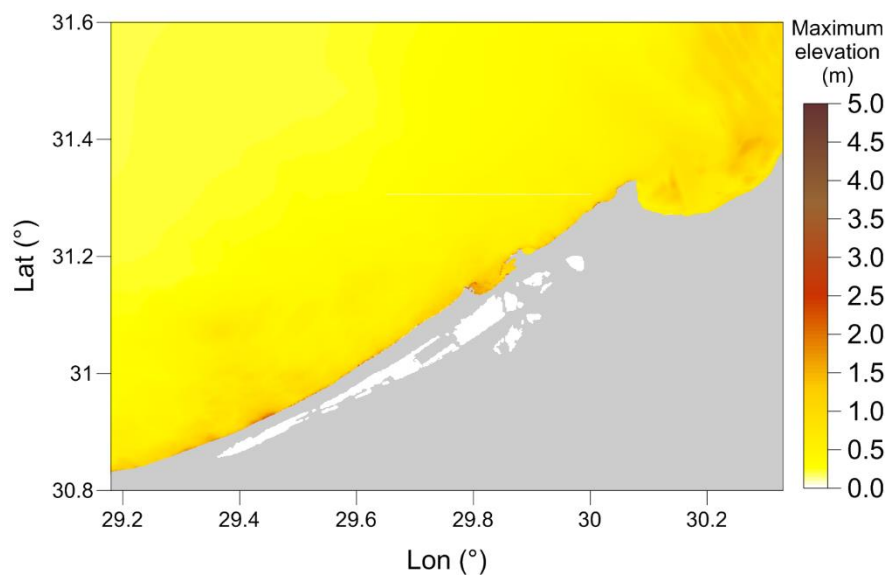
1110 Figure 12. Sea surface maxima for the CA source, zoomed in the area of Alexandria with grid

1111 3 (200 m resolution).

1112

47

Figure 13. Propagation fields for the CA tsunami scenario. Snapshots taken every 20 minutes. All fields are plotted in grid 2.

Figure 14. Water depth maxima on land for the CA case plotted in grid 4 (40 m resolution) in mean-sea-level conditions. See caption of Fig. 6 for further details.
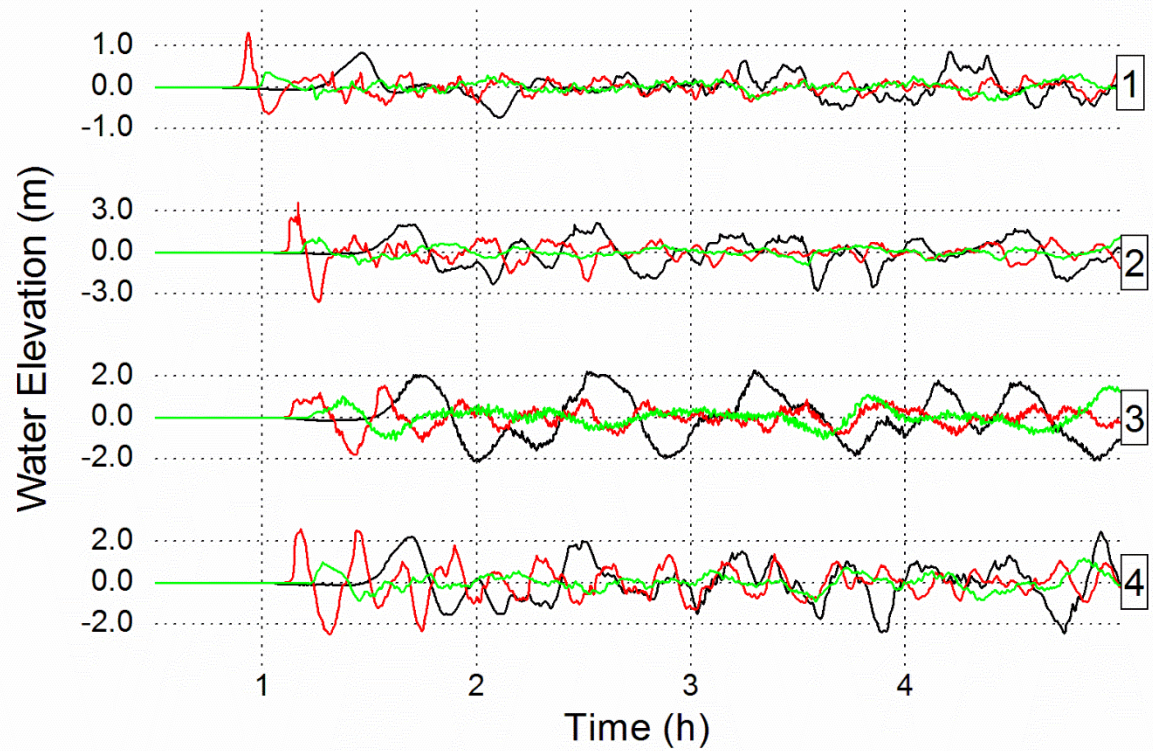
Figure 15. Time series calculated in the four positions shown in Figure 6 for mean-sea-level conditions: black line = WHA tsunami, red line = EHA tsunami, green line = CA tsunami.

Figure 16. Aggregate field of water depth maxima on land (grid 4), obtained by combining the results of the WHA, EHA and CA scenarios and superimposed on a Google Earth image. Tsunami simulations have been computed assuming mean-sea-level conditions.
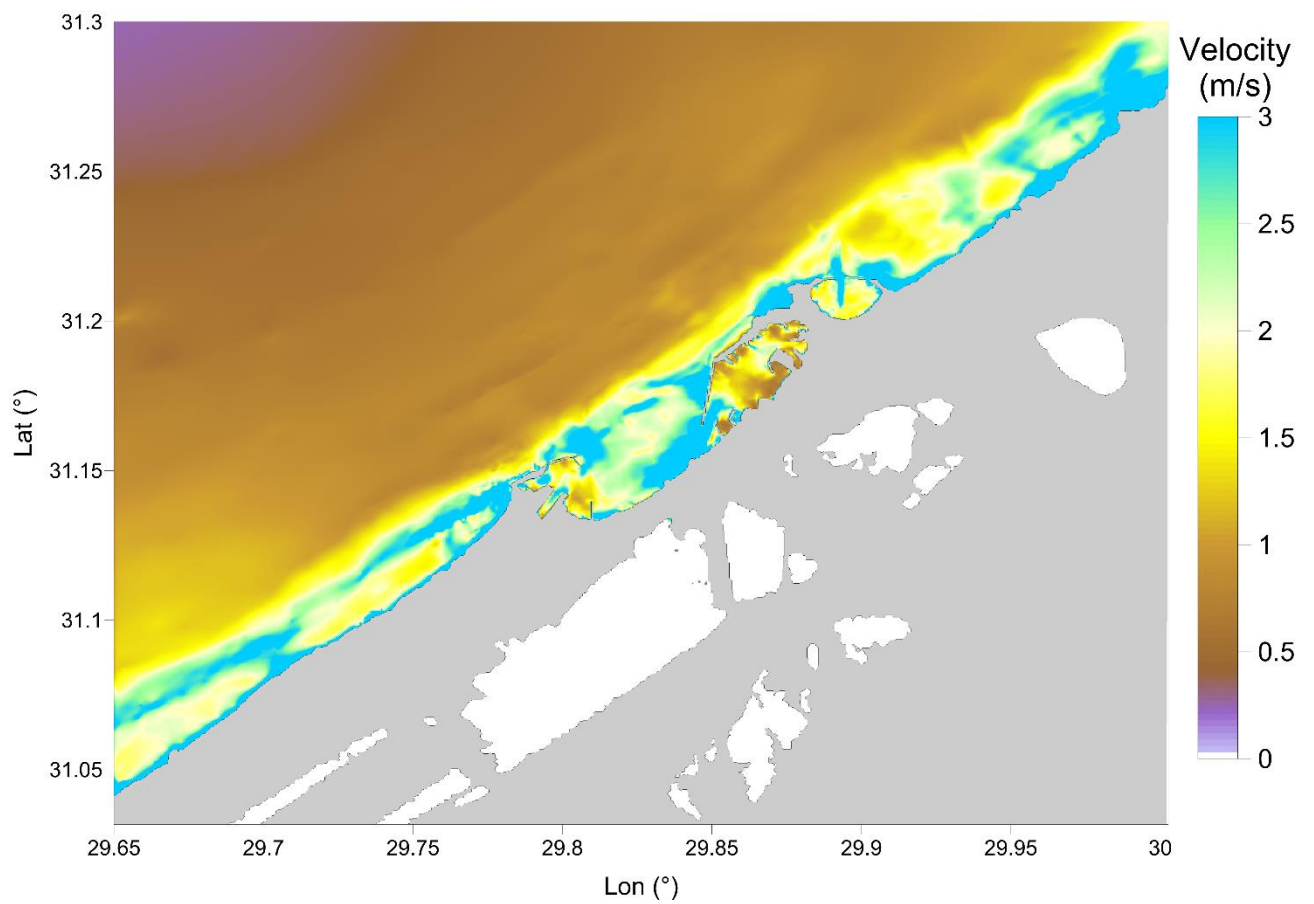
Figure 17. Aggregate field of velocity maxima calculated in the finest grid (40 m resolution) assuming mean-sea-level conditions.
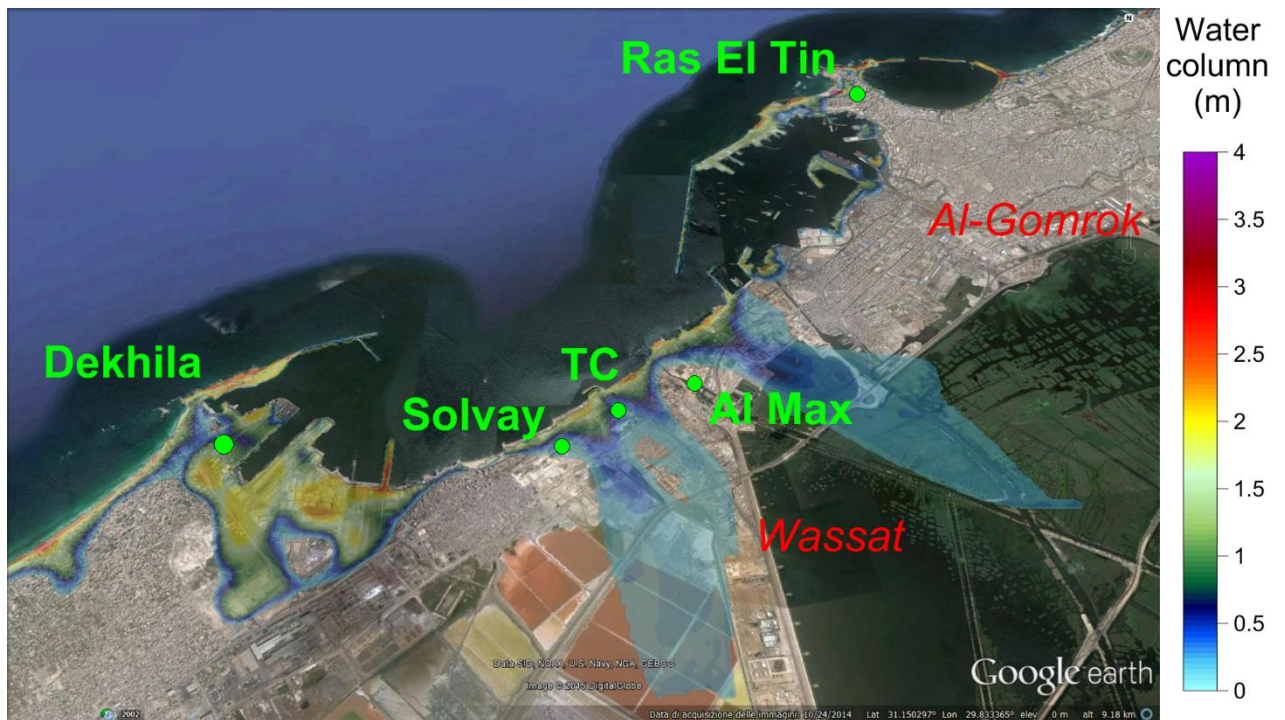
Figure 18. Zoom of the inundation area between the port of Dekhila and the port of Alexandria (covered by grid 4) under the assumption of tsunamis attacking in mean-sea-level conditions. A couple of toponyms and places of relevant industrial installations are also shown: Solvay = Alexandria Sodium Carbonate, TC = Titan Cement.

Figure 19. Map with meshes (80 m resolution) used for buildings vulnerability assessment focussed on the zone south-west of the Dekhila port. The green mesh covers the area of inundation, while the red one is a subset covering the area of Dekhila port (north) and the area of APC refinery (south) not considered for the vulnerability analysis. Assumption is made of mean-sea-level conditions.
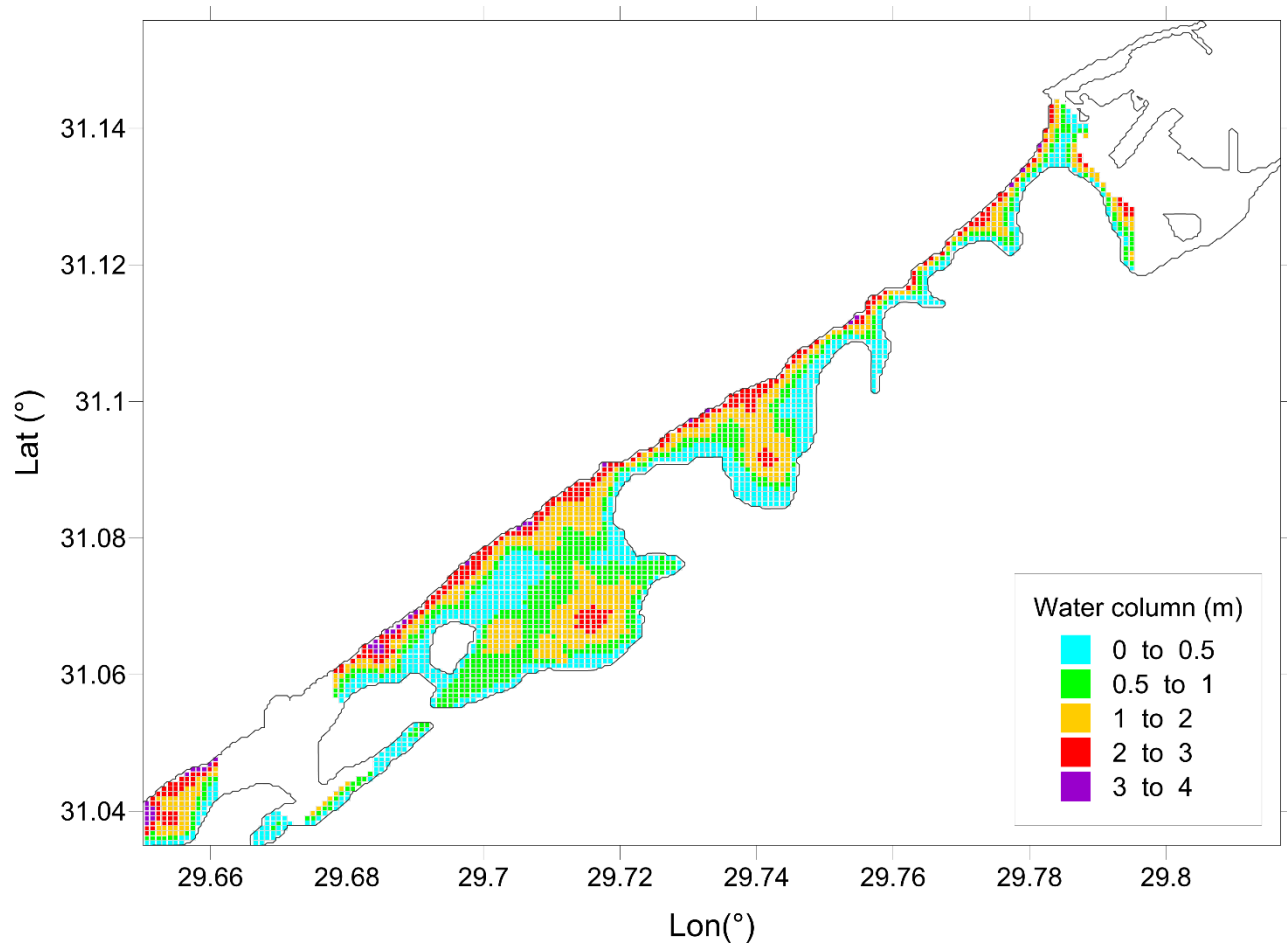
Figure 20. Tsunami flow depth under the mean-sea-level hypothesis in the zone to the south-west of the Dekhila port, discretized on the 80 m x 80 m cell tessellation that has been also used to assess the damage to the buildings.

1162

1163

1164 Figure 21. Typical constructions of classes from A to E in Alexandria (pictures from Google

1165 Earth database).

1166
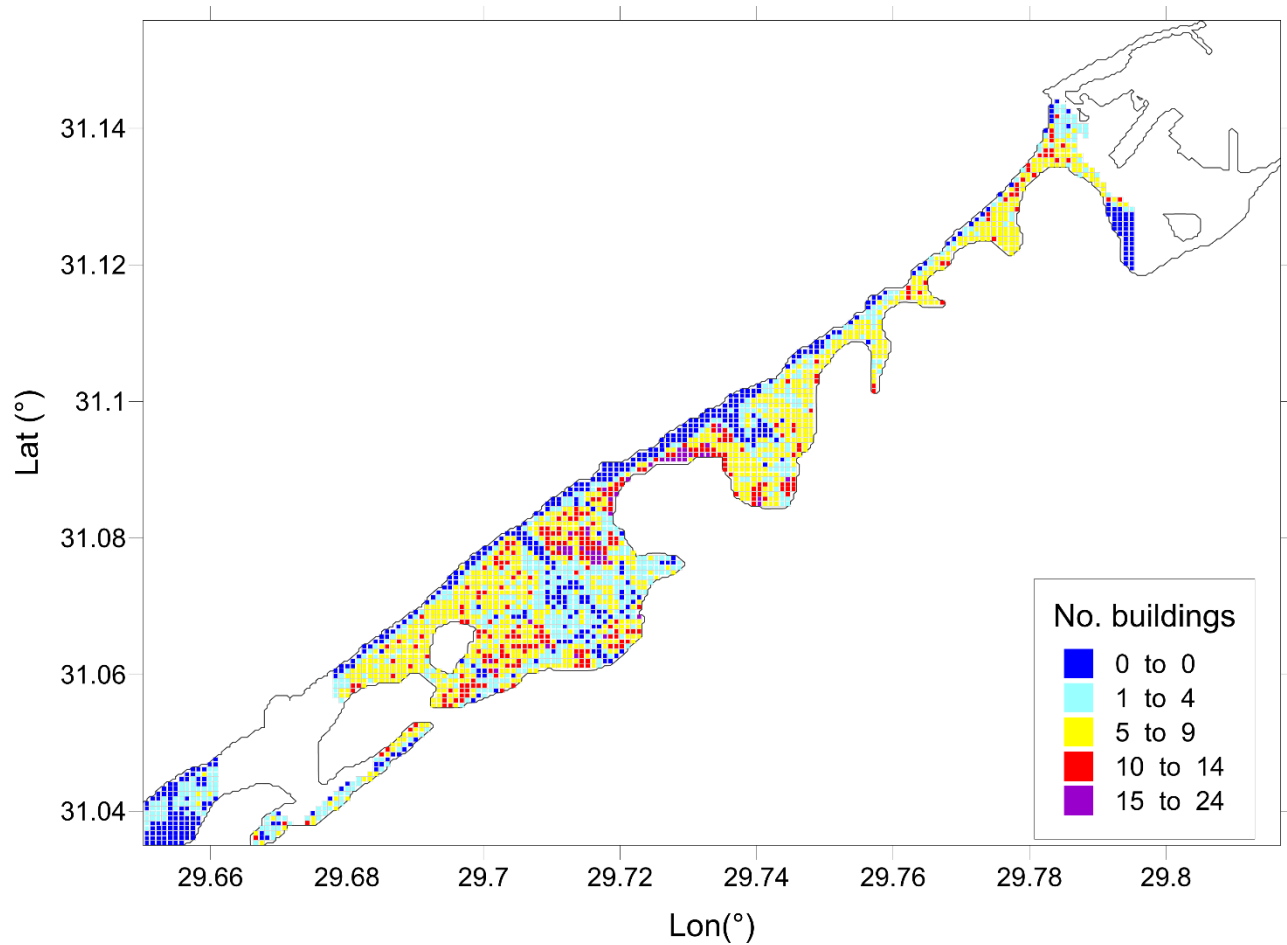
Figure 22. Map of the building density per cell for the 80x80 m tessellation. Most of the no-buildings cells are found along the shore or along stream banks. Most of cells are in the group 5-9 buildings per cell (yellow).

1174
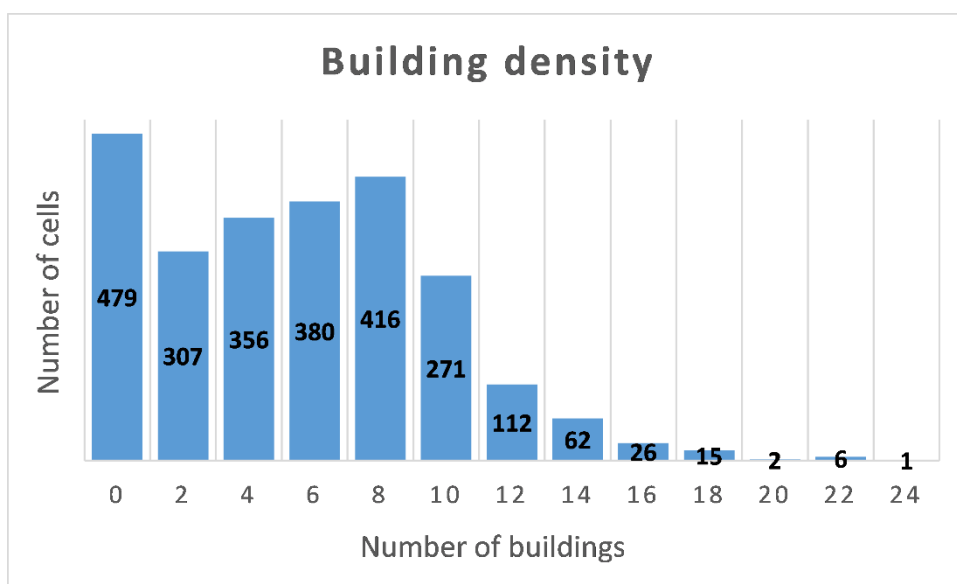
1175 Figure 23. Distribution of buildings per cell in the inundated area selected in step 2 (see text).

1176 Each class is denoted by an even number. All classes, but the first on the left, have width 2.

1177 This means that the column denoted with 2 contains all cells having either 1 or 2 buildings, the

1178 next denoted with 4 contains cells with 3 or 4 constructions, etc. Instead the first column

1179 contains only cells with no buildings. Figures in the columns are the number of cells.

1180

1181
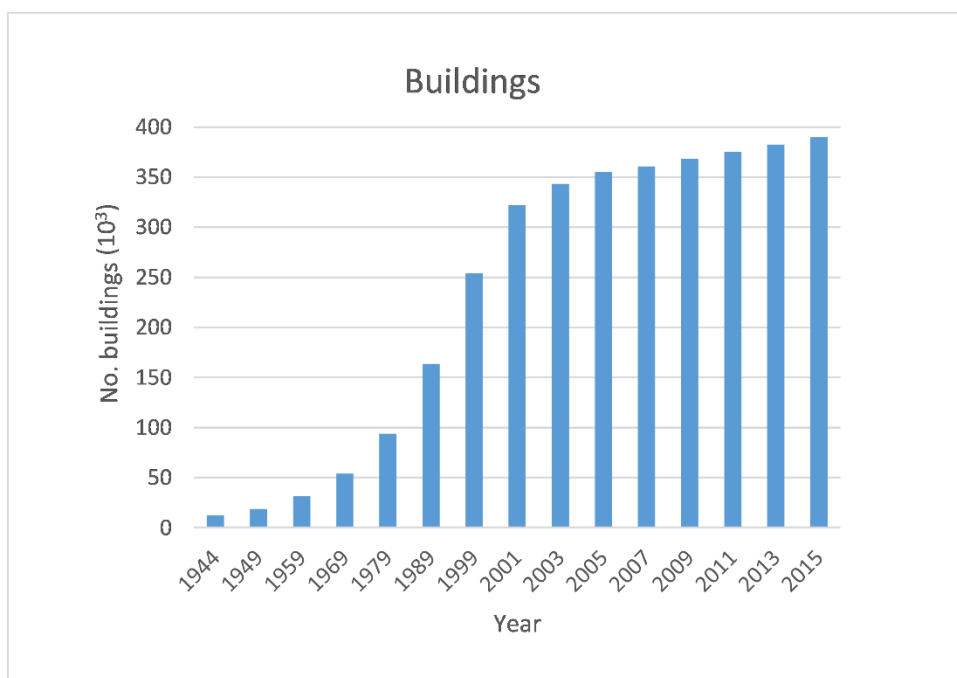
1182 Figure 24. Number of buildings in the Governorate of Alexandria from 1944 until 2015.

1183
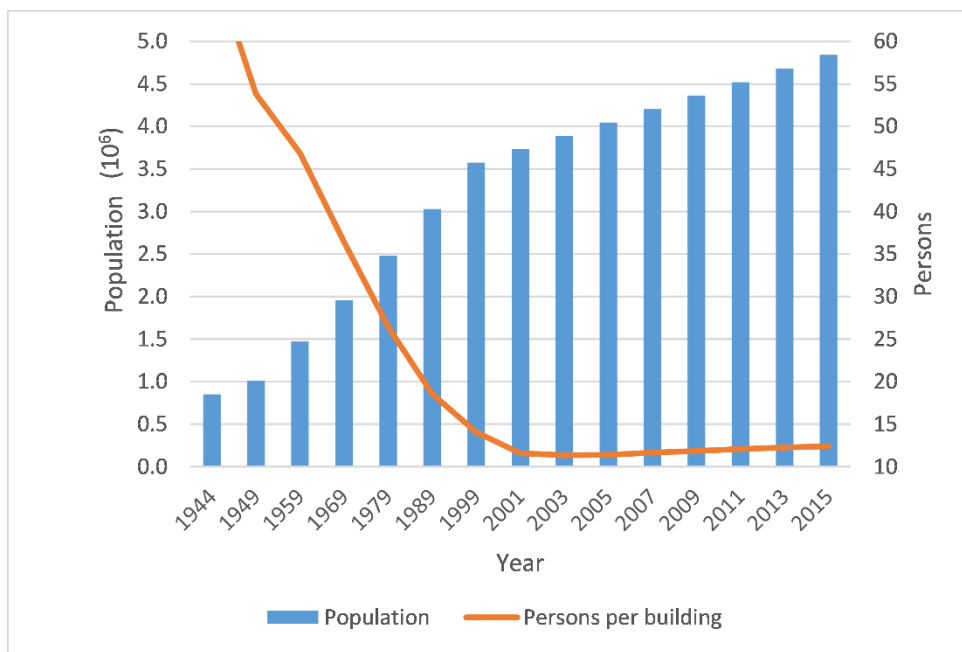
Figure 25. Population of the Governorate of Alexandria (histogram) and density of persons per buildings (continuous line) from 1944 until 2015.
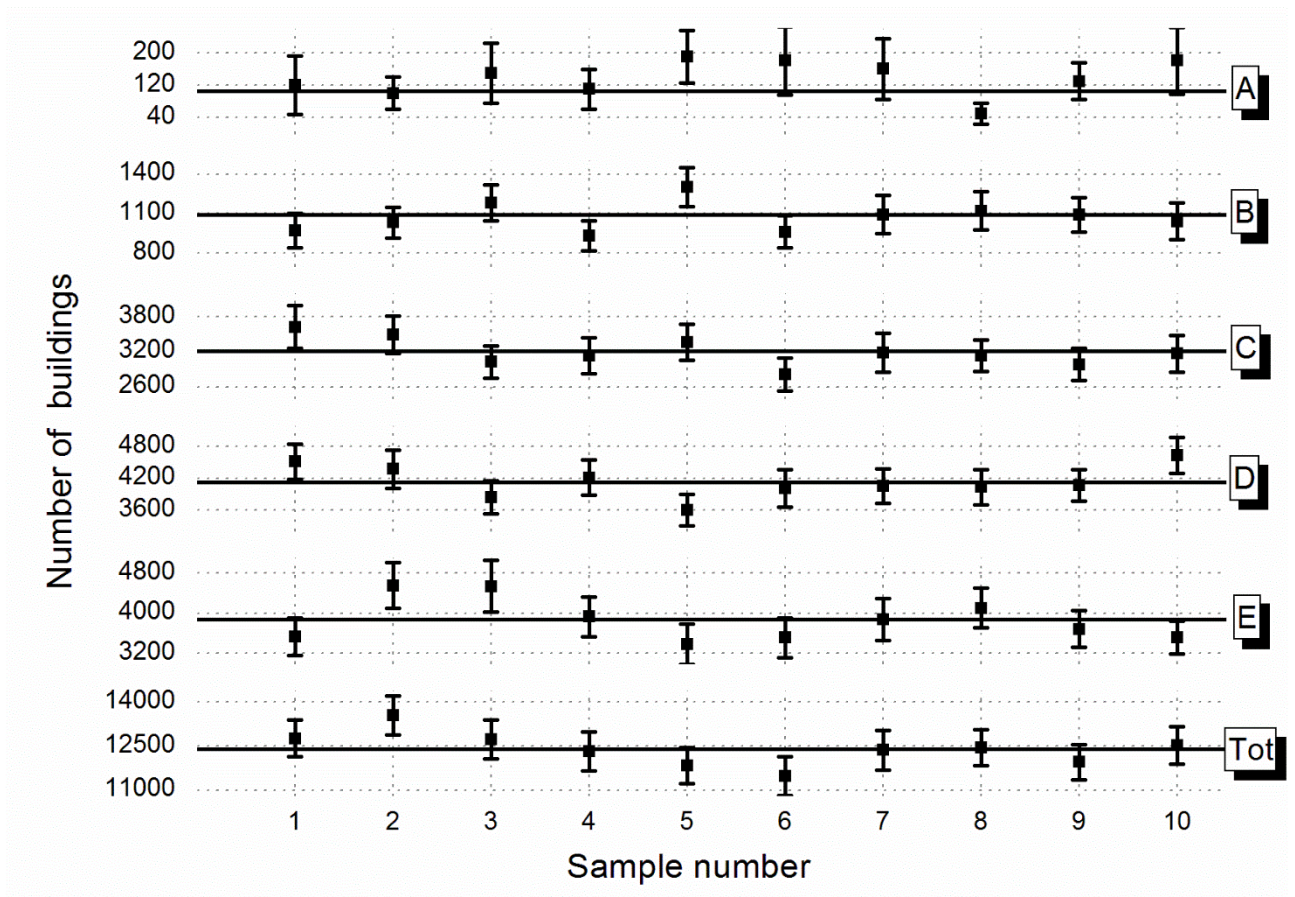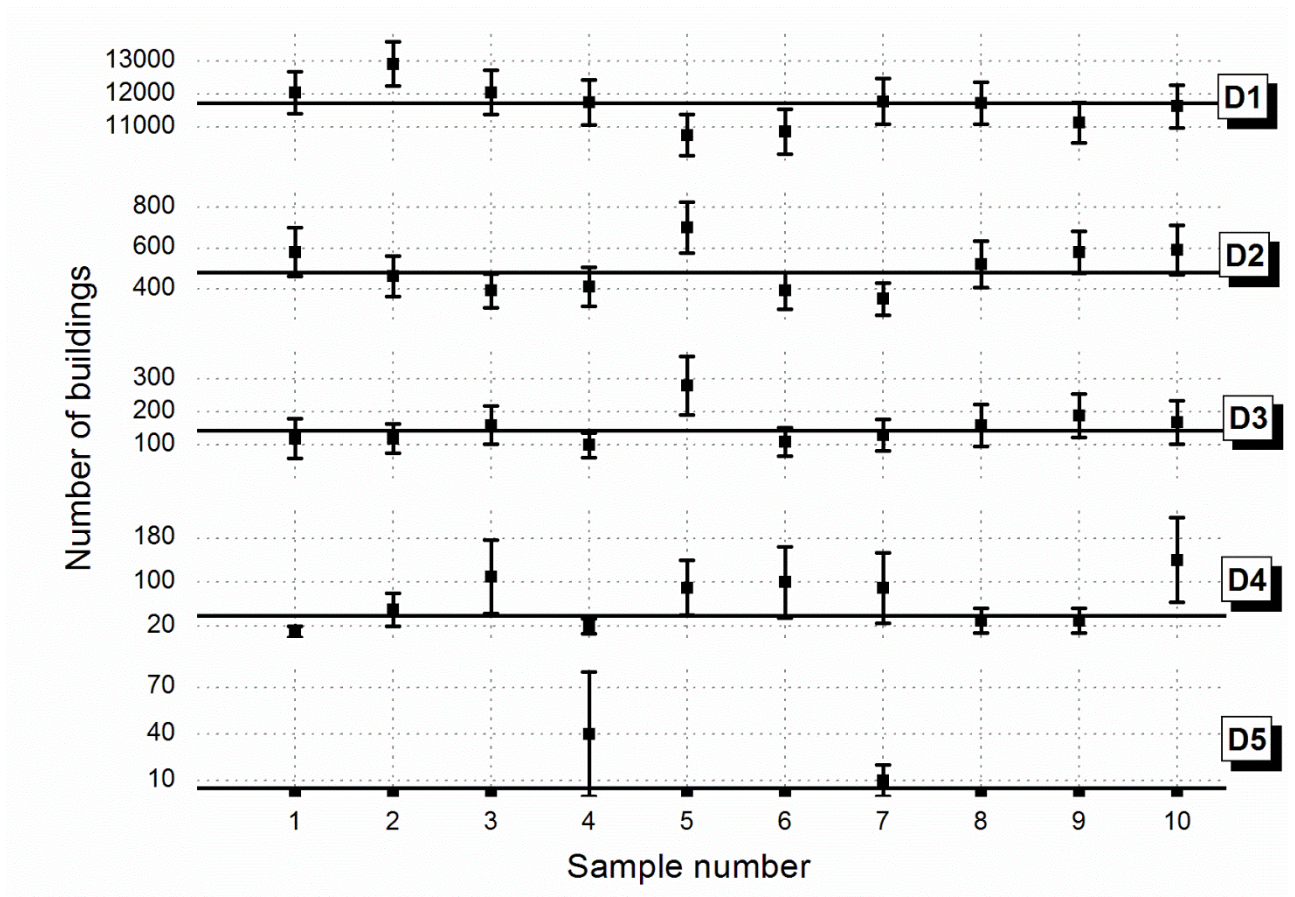
Figure A1. Number of buildings for each building type from A to E and total number of buildings for each of the 10 random, independent samples of cells (each containing 243 cells). The horizontal lines in each subplot corresponds to the value reported in Table 5 and referred to the full set of 2433 cells.

Figure A2. Number of buildings for each damage level from D1 to D5 for each of the 10 random, independent samples of cells (each containing 243 cells). The horizontal lines in each subplot corresponds to the value reported in Table 6, last row and referred to the full set of 2433 cells. Data refer to the mean-sea-level case.